

Submitted to *Transportation Science*  
manuscript

# A Unified Model for Multi-Task Drone Routing in Post-Disaster Road Assessment

Huatian Gong

School of Civil and Environmental Engineering, Nanyang Technological University, Singapore, [huatian.gong@ntu.edu.sg](mailto:huatian.gong@ntu.edu.sg)

Jiuh-Biing Sheu

Department of Business Administration, National Taiwan University, Taiwan, [jbsheu@ntu.edu.tw](mailto:jbsheu@ntu.edu.tw)

Zheng Wang

School of Maritime Economics and Management, Dalian Maritime University, China, [drwz@dlut.edu.cn](mailto:drwz@dlut.edu.cn)

Xiaoguang Yang

The Key Laboratory of Road and Traffic Engineering of the Ministry of Education, Tongji University, China, [yangxg@tongji.edu.cn](mailto:yangxg@tongji.edu.cn)

Ran Yan

School of Civil and Environmental Engineering, Nanyang Technological University, Singapore, [ran.yan@ntu.edu.sg](mailto:ran.yan@ntu.edu.sg)

Post-disaster road assessment (PDRA) is essential for emergency response, enabling rapid evaluation of infrastructure conditions and efficient allocation of resources. Although drones provide a flexible and effective tool for PDRA, routing them in large-scale networks remains challenging. Traditional optimization methods scale poorly and demand domain expertise, while existing deep reinforcement learning (DRL) approaches adopt a single-task paradigm, requiring separate models for each problem variant and lacking adaptability to evolving operational needs. This study proposes a unified model (UM) for drone routing that simultaneously addresses eight PDRA variants. By training a single neural network across multiple problem configurations, UM captures shared structural knowledge while adapting to variant-specific constraints through a modern transformer encoder-decoder architecture. A lightweight adapter mechanism further enables efficient finetuning to unseen attributes without retraining, enhancing deployment flexibility in dynamic disaster scenarios. Extensive experiments demonstrate that the UM reduces training time and parameters by a factor of eight compared with training separate models, while consistently outperforming single-task DRL methods by 6–14% and traditional optimization approaches by 24–82% in terms of solution quality (total collected information value). The model achieves real-time solutions (1–10 seconds) across networks of up to 1,000 nodes, with robustness confirmed through sensitivity analyses. Moreover, finetuning experiments show that unseen attributes can be effectively incorporated with minimal cost while retaining high solution quality. Validation on a real-world transportation network further demonstrates the model’s practical scalability. The proposed UM advances neural combinatorial optimization for time-critical applications, offering a computationally efficient, high-quality, and adaptable solution for drone-based PDRA.

*Key words:* Post-disaster road assessment, Drone routing, Deep reinforcement learning, Multi-task learning, Lightweight finetuning, Neural combinatorial optimization

## 1. Introduction

Disasters, such as earthquakes and hurricanes, pose severe threats to human lives, infrastructure, and economic stability (Avishan et al. 2023). In the immediate aftermath of such events, uncertainties regarding transportation infrastructure disruptions emerge, encompassing the extent of road network damage, operability, and feasibility of short-term restoration. Therefore, rapid assessment of road network damage is critical for effective emergency response, as it enables timely delivery of supplies, evacuation planning, and resource allocation (Zhang et al. 2023). This process, referred to as post-disaster road assessment (PDRA), is hindered by traditional ground-based methods, which are often impeded by impassable roads, hazardous conditions, and delays, making them impractical for time-sensitive disaster scenarios (Zhang et al. 2023, Gong et al. 2025). Unmanned aerial vehicles (or drones) have emerged as a transformative solution for PDRA, offering high mobility, rapid deployment, and the ability to capture high-resolution imagery in hazardous environments (Enayati et al. 2023, Shi et al. 2024, Steenbergen et al. 2025). Equipped with advanced sensors, drones can efficiently assess road damage severity, operability, and repair feasibility, providing critical data to guide relief efforts. Examples include their use in post-tsunami Haiyan (Ezequiel et al. 2015) and the Nepal earthquake (Abuali and Ahmed 2025).

Despite these advantages, solving drone routing for large-scale PDRA remains challenging. Traditional approaches, including exact methods (e.g., branch-and-bound algorithms) (Zhang et al. 2023, Yin et al. 2023, Morandi et al. 2024) and heuristic methods (e.g., simulated annealing) (Oruc and Kara 2018, Glock and Meyer 2020, Adsanver et al. 2025), suffer from significant limitations in real-world large-scale PDRA. These methods exhibit solution times that grow dramatically with problem complexity, making them ill-suited to time-critical disaster response where delays can be life-threatening. Moreover, developing effective solving algorithms requires extensive domain knowledge and substantial time investment in algorithm design. To address these two issues, Gong et al. (2025) proposed a deep reinforcement learning (DRL) approach for PDRA, which learns high-quality routing strategies directly from data without relying on domain knowledge, achieving real-time inference (1–10 seconds) and outperforming commercial solvers in solution quality. In recent years, DRL has been used to learn neural network-based heuristics for solving combinatorial optimization problems, receiving growing research attention for its potential to generate high-quality solutions with minimal human effort (Vinyals et al. 2015, Bello et al. 2016, Kool et al. 2018, Kwon et al. 2020, Luo et al. 2023, Zhou et al. 2024, Liu et al. 2024, Berto et al. 2024). However, this DRL method operates in a single-task paradigm, requiring a separate model for each specific PDRA variant. When problem characteristics change, such as variations in objective functions or constraints, a new model should be trained from scratch, leading to high computational

---

costs and deployment inefficiencies. Furthermore, the existing method lacks adaptability to unseen future attributes in evolving PDRA scenarios.

Inspired by advancements in large language models (LLMs), where a single model can be applied to diverse tasks with remarkable adaptability and deployment efficiency (Achiam et al. 2023, Touvron et al. 2023, Guo et al. 2025, Huang et al. 2025), this study extends the philosophy to neural combinatorial optimization for PDRA. The main contributions are summarized as follows:

- **Unified framework for multi-task PDRA.** We develop a unified model (UM) that simultaneously solves eight PDRA variants within a single architecture. Unlike existing traditional optimization and single-task DRL methods, which require separate models for each variant, UM leverages multi-task learning to capture shared structural knowledge while adapting to variant-specific constraints. This design reduces training time and parameter size by a factor of eight compared to training eight separate models, significantly improving computational efficiency and deployment feasibility.
- **Lightweight finetuning for unseen attributes.** We introduce an adapter layer mechanism that enables efficient finetuning of the pre-trained UM to incorporate new attributes (e.g., multi-depot settings). This mechanism preserves existing knowledge while adapting to new requirements with minimal computational cost, offering flexibility for rapidly evolving disaster response scenarios.
- **State-of-the-art performance and scalability.** Through experiments, we demonstrate that UM outperforms both traditional optimization (by 24–82%) and single-task DRL methods (by 6–14%) in terms of solution quality while maintaining real-time inference (1–10 seconds) for networks with up to 1,000 nodes. Sensitivity analyses confirm the model’s robustness under varying operational conditions, and validation on the real-world road network underscores the model’s practical scalability.

The remainder of this paper is organized as follows. Section 2 reviews the state-of-the-art in PDRA and related optimization approaches. Section 3 introduces the basic problem formulation. Section 4 outlines the PDRA variants and the motivation for a unified framework. Section 5 presents the proposed UM. Section 6 describes the adapter-based finetuning mechanism for new attributes. Section 7 reports numerical experiments. Finally, Section 8 concludes the paper and discusses future research directions.

## 2. Related work

PDRA has evolved with technological advancements. Traditional assessment methods, such as field surveys (Arii 2013) and satellite remote sensing (Bravo et al. 2019), are constrained by slow deployment, labor intensity, and low resolution, which hinder timely decision-making in crisis scenarios. To overcome these limitations, drones have emerged as a transformative solution for PDRA.

Drones offer strong mobility, cost efficiency, and high-resolution imaging capabilities, enabling rapid evaluation of road damage (e.g., cracks or landslides) and operability, thus becoming a cornerstone of modern PDRA (Enayati et al. 2023, Zhang et al. 2023).

A critical challenge in PDRA is solving drone routing for large-scale road networks. Existing approaches, including exact algorithms and metaheuristics, face two key limitations: computational inefficiency with increasing problem scale and heavy reliance on domain expertise in model and solution approach design (Gong et al. 2025, Jiang et al. 2025). For instance, Zhang et al. (2023) developed a branch-and-price model validated on 107-node road networks, but its solution time grows exponentially as scale increases. Similarly, Adsanver et al. (2025)'s heuristic approach, though effective for 148-node road networks, requires extensive domain knowledge and scales poorly for real-world large-scale PDRA. To address these issues, Gong et al. (2025) introduced a DRL framework for PDRA, leveraging an attention-based encoder-decoder model (AEDM). This method eliminates domain knowledge dependencies by learning routing strategies directly from data, achieving real-time inference (1–10 seconds) for networks with up to 1,000 nodes and outperforming commercial solvers by 16–69%.

Like vehicle routing problems with diverse variants (Luo et al. 2023, Zhou et al. 2024, Liu et al. 2024, Berto et al. 2024), PDRA involves multiple routing variants shaped by operational constraints: open routes (no depot return), time windows (temporal assessment constraints), and multi-depot scenarios (distributed launch points). However, existing methods, including exact algorithms, heuristics, and AEDM proposed by Gong et al. (2025), operate in a single-task paradigm, requiring separate models for each variant. Adapting to new constraints (e.g., switching from closed to open routes) necessitates full model redesign, leading to inefficiencies and limited adaptability to emerging PDRA scenarios. Table 1 compares these methods, highlighting gaps in unified modeling and adaptability. These approaches lack the ability to handle multiple variants or unseen attributes, underscoring the need for flexible frameworks that can address such limitations.

### 3. Preliminaries

In this section, we briefly introduce the PDRA using drones. For detailed elaboration, please refer to Gong et al. (2025). To maintain consistency and facilitate easy reference, we adopt their notation as much as possible. We first present the drone routing problem formulation, followed by the network transformation method and instance generation procedure.

#### 3.1. Drone routing

This study addresses the PDRA problem, wherein a fleet of  $K$  drones is deployed to assess the condition of road links. The road network is modeled as a graph  $G = (N, A)$ , where  $N$  denotes the set of nodes  $i, j \in N$  and  $A$  represents the set of links  $(i, j) \in A$  connecting these nodes. Let

**Table 1** Comparison of PDRA Methods

Authors	Objective	Method	Scale <sup>a</sup>	Efficiency		Uni.	Adpt.
				Time	Expert		
Oruc and Kara (2018)	Max. value & profit	Base route heuristic	44	Slow	Yes		
Glock and Meyer (2020)	Max. info. in time	Neighborhood search	625	Slow	Yes		
Zhang et al. (2023)	Max. reward	Branch-and-price	107	Slow	Yes		
Yin et al. (2023)	Min. cost	Branch-and-price	45	Slow	Yes		
Morandi et al. (2024)	Max. prize	Branch-and-cut	50	Slow	Yes		
Adsanver et al. (2025)	Max. priority	Variable neighborhood	148	Slow	Yes		
Gong et al. (2025)	Max. reward	DRL (AEDM)	1,000	Fast	No		
<b>This study</b>	<b>Max. reward</b>	<b>Unified DRL</b>	<b>1,000</b>	<b>Fast</b>	<b>No</b>	✓	✓

<sup>a</sup>Number of nodes in the road network.

$t_{ij}$  denote the time required for a drone to assess link  $(i, j)$ , and  $c_{ij}$  denote the information value derived from such assessment. The objective is to determine optimal assessment routes for  $K$  drones to maximize the total value of information collected across network links.

Each drone is equipped with high-definition cameras and operates under three critical constraints for PDRA. First, each drone has a battery-imposed flight time limit  $Q$ . Second, the entire assessment operation must be completed within a maximum allowable time  $p_{\max}$ . Third, due to operational altitude and visual range limitations, a bidirectional road link can only be assessed if a drone flies directly along it (Zhang et al. 2023). The PDRA problem involves two distinct time considerations: the computational time to generate assessment routes and the operational time for drones to execute those routes.

A challenge in PDRA formulation is the dual-network structure required for efficient drone operations. As illustrated in Figure 1(a), the dual-network setup comprises two distinct structures: the original road network  $G$  where drones assess individual link damage (shown as solid blue lines), and a fully connected auxiliary network  $G' = (N, A')$  where every node is directly connected to all other nodes (shown as dashed red lines). This auxiliary network enables drones to bypass physical road links for faster transit between assessment locations, balancing thorough damage assessment with the time-sensitive requirements of PDRA.

### 3.2. Network transformation

To resolve the ambiguities in the dual-network formulation, where both road links and direct routes may connect the same pair of nodes, Gong et al. (2025) developed a network transformation method tailored for PDRA, converting the link-based routing problem into an equivalent node-based formulation. This transformation, illustrated in Figure 1(b), involves splitting each road link  $(i, j) \in A$  by introducing an artificial node  $p \in P$ , creating two new links:  $(i, p)$  and  $(p, j)$ . The

transformation process converts the dual network  $G'' = (N, A + A')$  into a reduced network  $\bar{G} = (\bar{N}, \bar{A}) = (N \cup P, 2A \cup A')$ , where  $|P| = |A|$ . In the transformed network, the ambiguity of multiple edges between nodes is resolved to support accurate PDRA: traversing  $(i, p)$  and  $(p, j)$  corresponds to assessing the original link  $(i, j)$ , while direct links in  $A'$  remain unchanged for transit purposes. As shown in Figure 1(c) and (d), the information value of artificial node  $p$  is set as  $c_p = c_{ij}$ , and the traversal time is split as  $t_{ip} = t_{pj} = t_{ij}/2$ , effectively converting the link-based PDRA routing problem into a node-based problem.

This transformation allows the PDRA problem to be formulated as a variant of the orienteering problem where artificial nodes in  $P$  carry information values (prizes) and must be visited to collect damage assessment data, while original nodes in  $N$  serve as waypoints for routing. However, critical differences exist from standard orienteering problems to accommodate PDRA needs: (1) original nodes in  $N$  carry no information value, (2) artificial nodes in  $P$  are isolated from each other and connect only to specific nodes in  $N$ , and (3) artificial nodes in  $P$  are exclusive (each can be visited by only one drone) to avoid redundant assessments, whereas nodes in  $N$  can be revisited, enabling loop formations in drone paths to enhance PDRA efficiency.

### 3.3. Instance generation

Because large-scale real-world road network datasets suitable for training deep learning models are scarce, Gong et al. (2025) developed a synthetic road network generation method specifically tailored for drone routing problems in PDRA. The generation process follows a four-stage pipeline: (1) *Grid Network Initialization*, which creates a uniform square grid of  $N$  nodes over the coordinate space  $[0, 1]^2$ ; (2) *Link Pruning*, which randomly removes edge subsets while maintaining network connectivity to simulate real-world road networks; (3) *Node Perturbation*, which introduces bounded random perturbations to node coordinates to avoid regularity, ensuring the synthetic networks better reflect the irregularities of actual road networks; and (4) *Attribute Assignment*, which computes Euclidean lengths for remaining edges and assigns random damage information values to transformed artificial nodes.

## 4. Variants and motivations

Drone routing for PDRA encompasses diverse problem variants, each reflecting unique operational constraints or environmental realities in post-disaster scenarios. These variants as listed below extend the preliminary PDRA (Gong et al. 2025) and shape the need for a UM to enhance practical applicability.

- a) **Open Routes (OR).** In standard PDRA formulations, drones return to a depot after completing routes (closed routes). However, post-disaster scenarios may require open routes where

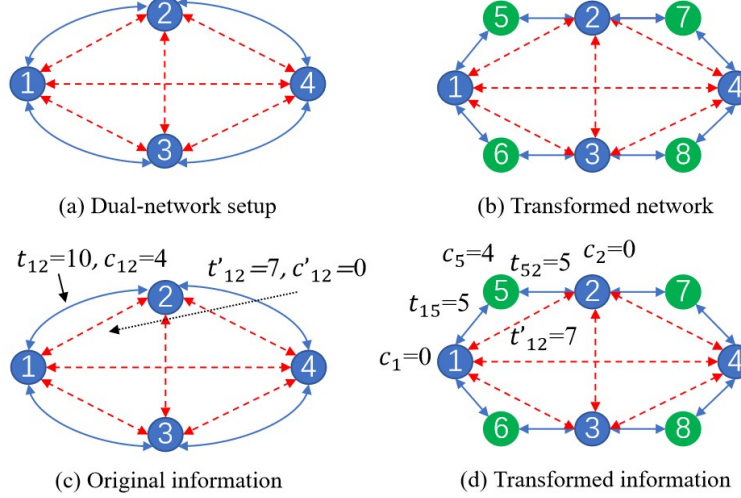


**Figure 1 Dual-Network Structure and Transformed Node-Based Representation**

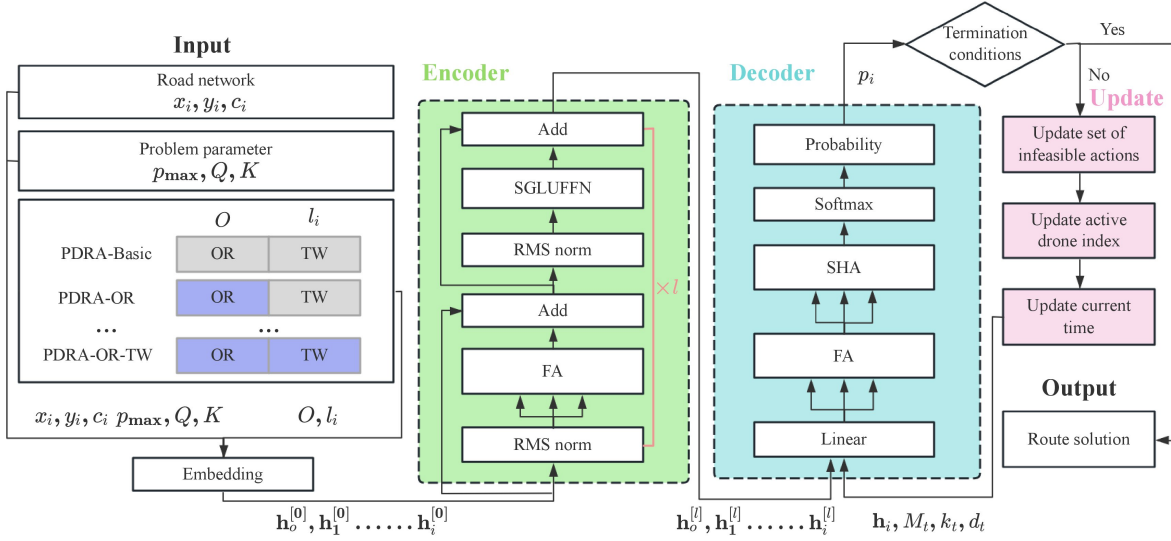
drones may land at temporary sites instead of returning to the original depot. This configuration prioritizes the rapid collection of road condition data over mandatory depot return, thereby optimizing the operational efficiency of PDRA missions.

- b) **Time Windows (TW).** Road links in PDRA may have time windows with latest allowable assessment times  $l_{ij}$  (where  $l_{ij}$  denotes the late time window for link  $(i,j)$ ) reflecting when assessment must be completed to remain valuable. For instance, operational priorities in PDRA might require critical links (e.g., hospital access roads) to be assessed within the first assessment phase. Drones would need to traverse link  $(i,j)$  before time  $l_{ij}$  to collect valid PDRA data, adding temporal feasibility checks that could complicate path sequencing.
- c) **Multi-Depots (MD).** Large disaster zones in PDRA may have multiple depots (e.g., fire stations or emergency camps) where drones can launch. Formally, let  $D \subseteq N$  be a set of depots ( $|D| \geq 2$ ); drones might start at a depot  $d \in D$  and may return to the depot (or none, for the open route) to streamline PDRA operations across vast areas.

The above variants create distinct problem structures for PDRA. The presence or absence of the three attributes results in 8 variants as shown in Table 2. Existing methods, including exact methods, heuristics, and AEDM proposed by Gong et al. (2025), operate in a single-task paradigm, requiring separate models for each PDRA variant, which hinders practical deployment. A UM capable of solving all PDRA variants within a single model addresses these shortcomings by reducing computational overhead and improving deployment flexibility. Moreover, operational environments may introduce future, previously unseen attributes in evolving PDRA scenarios. In this study, MD is deliberately regarded as such a future attribute for PDRA. After training UM (discussed in Section 5), the attribute can be incorporated via a lightweight adapter layer mechanism (discussed

**Table 2 PDRA Problem Variants by Attribute Combinations**

Variant	Open Route (OR)	Time Window (TW)	Multi-depots (MD)
PDRA-Basic			
PDRA-OR	✓		
PDRA-TW		✓	
PDRA-OR-TW	✓	✓	
PDRA-MD			✓
PDRA-OR-MD	✓		✓
PDRA-TW-MD		✓	✓
PDRA-OR-TW-MD	✓	✓	✓

**Figure 2 Overall Model Architecture for Unified Multi-variant PDRA**

in Section 6), enabling efficient finetuning without full retraining. This design ensures adaptability to evolving post-disaster response requirements, a critical feature for robust PDRA systems.

## 5. Development of the unified model

### 5.1. Model architecture

The overall model architecture is illustrated in Figure 2, which depicts a unified framework capable of handling multiple PDRA variants through a modern encoder-decoder structure. The architecture comprises five main components: input, encoder, decoder, update and output. Each component is detailed in the following subsections.

**5.1.1. Input** The input to the model consists of three main parts: road network data, problem parameters, and problem attributes. For any real-world road network, each node  $i \in N$  is linked with geographic coordinates  $(x_i, y_i)$  and the corresponding lengths of the connected roads. Through the network transformation method outlined in Section 3.2, the dual-network structure is converted into an equivalent node-based network. In this transformed network, every node  $i \in \bar{N}$  has clearly

defined coordinates  $(x_i, y_i)$  and information values  $c_i$ . Problem parameters include operational constraints: maximum assessment time  $p_{\max}$ , battery flight time limit  $Q$ , and number of available drones  $K$ . The problem attributes cover OR and TW, while MD is treated as an unseen attribute (discussed in Section 6). During training, the OR attribute is represented by a binary scalar  $O$  ( $O = 0$  indicates an open route, and  $O = 1$  indicates a closed route). For the TW attribute, since the link-based problem is transformed into a node-based equivalent, the latest time windows  $l_{ij}$  specific to each link are also transformed into node-specific values  $l_i$ . To enhance the model's robustness, the OR and TW attributes are activated independently in each training batch: the value of  $O$  is set to 0 or 1 with an equal probability of 50%; and the time windows are either set to their actual values or to  $l_i = \infty$  (meaning that this TW attribute is not considered) with an equal probability of 50%. An embedding layer is used to map raw node features into a latent space, and the nodes are categorized into two types:

a) **Road network nodes** ( $\bar{N}$ ): these include the original nodes ( $N$ ) and artificial nodes ( $P$ ).

Each node  $i \in \bar{N}$  is defined by its coordinates  $(x_i, y_i)$  and information value  $c_i$ , where  $c_i = 0$  for nodes  $i \in N$  and  $c_i > 0$  for artificial nodes  $i \in P$ . The initial embeddings are calculated as follows:

$$\mathbf{h}_i^{[0]} = [x_i, y_i, c_i, l_i] \mathbf{W} + \mathbf{b}, \quad \forall i \in \bar{N}, \quad (1)$$

where  $[ \cdot ]$  stands for feature concatenation,  $\mathbf{W} \in \mathbb{R}^{4 \times d}$  and  $\mathbf{b} \in \mathbb{R}^d$  are learnable parameters, and  $\mathbf{h}_i^{[0]} \in \mathbb{R}^d$  represents the initial embedding of node  $i$ .

b) **Depot node** ( $o$ ): this node acts as both the starting point and the end point, and it combines its coordinates  $(x_o, y_o)$  with global parameters  $(p_{\max}, Q, K, O)$ :

$$\mathbf{h}_o^{[0]} = [x_o, y_o, p_{\max}, Q, K, O] \mathbf{W}_o + \mathbf{b}_o, \quad (2)$$

where  $\mathbf{W}_o \in \mathbb{R}^{6 \times d}$  and  $\mathbf{b}_o \in \mathbb{R}^d$  are learnable parameters specific to the depot node, resulting in the initial embedding  $\mathbf{h}_o^{[0]} \in \mathbb{R}^d$ .

This heterogeneous embedding approach clearly differentiates between node types and incorporates global operational constraints into the depot node's representation, thereby providing a unified feature space for subsequent processing.

**5.1.2. Encoder** The encoder converts embedded input features into high-level contextual representations through a stack of  $l$  transformer layers. In the traditional transformer encoder (Vaswani et al. 2017, Kool et al. 2018, Kwon et al. 2020, Luo et al. 2023, Zhou et al. 2024, Liu et al. 2024), each layer consists of two sublayers: (1) a multi-head attention (MHA) mechanism that models pairwise interactions between nodes, and (2) a position-wise feed-forward network (FFN)

that independently refines the representation of each node. Each sublayer is followed by residual connections and instance normalization to ensure stable training and improved generalization. However, traditional transformer architectures face computational inefficiencies when processing large-scale routing problems, particularly in terms of memory usage and training stability. The standard attention mechanism exhibits quadratic complexity with sequence length, while conventional normalization techniques may not provide optimal gradient flow for deep networks. Additionally, traditional ReLU-based FFN have limited expressiveness for capturing complex non-linear relationships in routing optimization. To address these issues, our model adopts a modern transformer encoder (Berto et al. 2024), inspired by advancements in LLM (Nguyen et al. 2024, Dubey et al. 2024), with four key enhancements (illustrated in Figure 3):

- a) Root Mean Square (RMS) normalization replaces instance normalization, providing better training stability and reducing computational overhead (Zhang and Sennrich 2019).
- b) Pre-normalization configuration shifts the normalization step to before residual connections, enhancing gradient flow and accelerating convergence (Jiang et al. 2023).
- c) FlashAttention (FA) is used in all MHA layers to improve efficiency when processing large input graphs without losing numerical accuracy (Dao et al. 2022, Dao 2023).
- d) Swish Gated Linear Unit Feed-Forward Network (SGLUFFN), an extension of the Gated Linear Unit (Dauphin et al. 2017), replaces the traditional ReLU-based FFN, strengthening the model’s ability to capture complex non-linear relationships (Shazeer 2020).

Formally, for node  $i \in \bar{N}$  and depot node  $o$ , the computations in the  $l$ -th encoder layer are as follows:

$$\bar{\mathbf{h}}_i = \text{RMS}(\mathbf{h}_i^{[l]}), \quad (3)$$

$$\hat{\mathbf{h}}_i = \mathbf{h}_i^{[l]} + \text{FA}(\bar{\mathbf{h}}_o, \bar{\mathbf{h}}_1, \dots, \bar{\mathbf{h}}_i), \quad (4)$$

$$\mathbf{h}_i^{[l+1]} = \hat{\mathbf{h}}_i + \text{SGLUFFN}(\text{RMS}(\hat{\mathbf{h}}_i)), \quad (5)$$

where  $\mathbf{h}^{[l]} \in \mathbb{R}^d$  denotes the input vector to the  $l$ -th layer. Detailed formulations of RMS, FA and SGLUFFN are in Appendix 8, and ablation studies in Appendix Equation (8) validate the superiority of this modern architecture over traditional transformers.

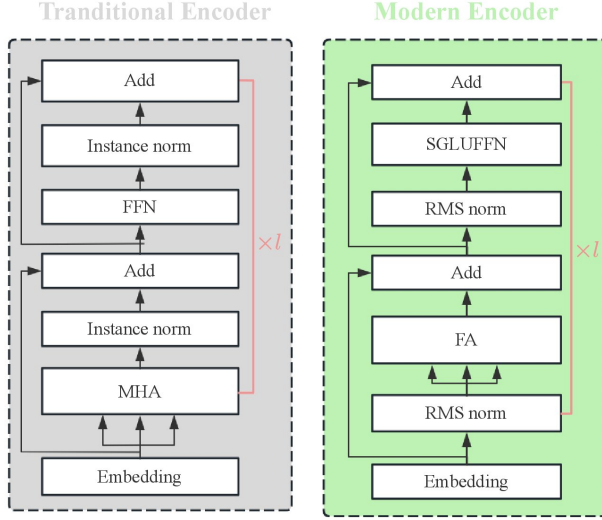


**Figure 3 Comparison between the Traditional Transformer Encoder Architecture and the Proposed Modern Encoder**

**5.1.3. Decoder** The decoder's main role is to build solutions step by step by fusing the final output embeddings  $\mathbf{h}_i^{[l]}$  from the encoder with the current state representation at each time step  $t$ . A context embedding mechanism adjusts the query space dynamically by merging the embedding of the current problem node with relevant state details. This context embedding  $\mathbf{h}_c^{(t)}$  is obtained through a linear projection of combined features: the node embedding from the encoder's last layer ( $\mathbf{h}_i^{[l]}$ ) and dynamic state features like the current time  $d_t$  and the index  $k_t$  of the active drone. In mathematical terms:

$$\mathbf{h}_c^{(t)} = \begin{cases} [\mathbf{h}_i, d_t, k_t] \mathbf{W}_c + \mathbf{b}_c & t \geq 1, \\ [\mathbf{h}_o, d_t, k_t] \mathbf{W}_c + \mathbf{b}_c & t = 0. \end{cases} \quad (6)$$

Here,  $\mathbf{h}_i$  is the final-layer encoder embedding of the node chosen at the previous time step  $i$ ;  $\mathbf{h}_o$  is the depot embedding from the encoder's final layer;  $d_t$  and  $k_t$  respectively capture the temporal state and the index of the active drone; and  $\mathbf{W}_c \in \mathbb{R}^{(d+2) \times d}$  and  $\mathbf{b}_c \in \mathbb{R}^d$  are learnable projection parameters. For clarity, the encoder layer index is omitted, and all variables from the encoder refer to the output of the final encoder layer  $[l]$ . This context embedding setup helps the decoder keep track of both the current solution state and operational constraints when generating subsequent actions. By explicitly including the temporal progression ( $d_t$ ) and drone index ( $k_t$ ), the model can adapt its decision policy according to the changing characteristics of the solution across different PDRA variants. Subsequently, the FA layer and a single-head attention (SHA) layer are utilized, expressed as:

$$\bar{\mathbf{h}}_c^{(t)} = \text{FA} (\mathbf{h}_c^{(t)}, \mathbf{h}_o, \mathbf{h}_1, \mathbf{h}_2, \dots, \mathbf{h}_i, M_t), \quad (7)$$

$$\mathbf{u} = u_o, u_1, \dots, u_i = \text{SHA} (\bar{\mathbf{h}}_c^{(t)}, \mathbf{h}_o, \mathbf{h}_1, \mathbf{h}_2, \dots, \mathbf{h}_i, M_t), \quad (8)$$

where  $M_t$  represents the set of infeasible actions at the current time step  $t$ , which will be elaborated on later. The probability of selecting node  $i$  at time step  $t$  is calculated using the softmax function:

$$p_i = \text{Softmax}(C \cdot \tanh(\mathbf{u})), \quad (9)$$

where  $C$  acts as a clipping parameter for the  $\tanh$  function, boosting solution exploration in the search space (Bello et al. 2016, Berto et al. 2024). Once the probability distribution  $p_i$  is obtained, the current time step  $t$  is concluded, and the state is updated to  $t + 1$ , enabling the decoder to build solutions in an autoregressive manner that adapts to diverse PDRA variants. Detailed mathematical formulations of SHA and Softmax are also provided in Appendix 8.

At each decoding step  $t$ , the decoder generates a probability distribution  $p_i$  over the set of feasible nodes, representing the likelihood of selecting node  $i$  as the next visiting location. Sampling or greedy selection based on  $p_i$  sequentially constructs a drone's route. Formally, the decoder outputs a solution  $\Pi = (\pi^1, \pi^2, \dots, \pi^K)$ , where  $\pi^k = (\pi_1^k, \pi_2^k, \dots, \pi_t^k)$  denotes the ordered sequence of nodes visited by drone  $k$ . Each route starts from the depot, visits a subset of nodes, and terminates according to the variant-specific constraints and route type (closed or open routes for OR attribute).

**5.1.4. Update** The update mechanism maintains solution feasibility and tracks the routing state across decoding steps. Two key components are updated at each time step  $t$ : (1) the set of infeasible actions  $M_t$  to ensure constraint compliance, and (2) the system state variables including the active drone index  $k_t$  and current time  $d_t$ . These updates enable the decoder to generate valid solutions across all PDRA variants while adapting to their specific operational constraints.

*Infeasible actions for  $M_t$ .* The decoder employs a masking mechanism that sets  $u_i = -\infty$  for infeasible actions at time step  $t$ . The set of infeasible actions  $M_t$  includes the following categories, tailored to handle the attributes of PDRA variants (OR and TW):

- Network connectivity constraint: The next node is not connected to the current node at time step  $t$  in the transformed road network. This masking ensures that the decoder's output adheres to the routing rules of the road network.
- Information collection constraint: Nodes with damage information values (i.e., belonging to the set  $P$ ) that have been visited at the current time step  $t$  are masked. This masking prevents redundant collection of damage information values from links.
- Time window constraint: For problems with the TW attribute, nodes are masked if they cannot be visited within their specified time windows. Specifically, node  $i$  is masked if  $d_t + t_{ji} > l_i$ , where  $d_t$  is the current time,  $t_{ji}$  is the travel time from the previous node  $j$  to node  $i$ , and  $l_i$  represents the latest allowable time window for node  $i$ .

- d) Flight time and battery constraints: Each drone must complete its mission within the specified assessment time limit  $p_{\max}$  and battery flight time limit  $Q$ . The masking rules are determined by both the route type (OR attribute) and node characteristics.
  - d1) For closed routes, when the next candidate node  $i \in N$  (network nodes without damage information) is connected to the depot, node  $i$  is masked if  $d_t + t_{ji} + t_{io} > \min(p_{\max}, Q)$ , where  $t_{io}$  denotes the return flight time from node  $i$  to depot  $o$ . When the candidate node  $i \in P$  (artificial nodes with damage information) is not directly connected to the depot, it is masked if  $d_t + 2t_{ji} + t_{io} > \min(p_{\max}, Q)$ , where the coefficient 2 accounts for the traversal time splitting described in Section 3.2.
  - d2) For open routes, the masking conditions simplify as depot return is not required. Specifically, nodes  $i \in N$  are masked when  $d_t + t_{ji} > \min(p_{\max}, Q)$ , while nodes  $i \in P$  are masked when  $d_t + 2t_{ji} > \min(p_{\max}, Q)$ .

These masking mechanisms collectively ensure adherence to the transformed network's structural constraints, prevent redundant information collection, enforce temporal feasibility, and maintain operational time limits across both open and closed route configurations, thereby guaranteeing feasible drone routing solutions for all PDRA variants.

*Active drone index for  $k_t$ .* After each node selection, the decoder updates the system state to maintain consistency across multi-drone operations, accommodating varying fleet sizes without requiring variant-specific adjustments. The update rule for the active drone index  $k_t$  is designed to handle both closed and open route configurations:

$$k_{t+1} = \begin{cases} k_t + 1 & \text{if route termination condition is met} \\ k_t & \text{otherwise} \end{cases}, \quad (10)$$

where route termination is defined as the selected node being the depot  $o$  for the closed route, or the drone having completed its maximum allowable mission time or visited all accessible nodes for the open route.

*Current time for  $d_t$ .* The current time  $d_t$  is updated using the same route termination condition as defined above, ensuring temporal consistency across all variants:

$$d_{t+1} = \begin{cases} 0 & \text{if route termination condition is met} \\ d_t + t_{ji} & \text{otherwise} \end{cases}. \quad (11)$$

**5.1.5. Output** The decoder produces a feasible solution  $\Pi = (\pi^1, \pi^2, \dots, \pi^K)$  and terminates based on route-type-specific criteria. For closed routes, termination occurs when either all  $K$  drones have completed their routes by returning to the depot, or all assessable nodes in  $P$  have been visited and the active drone returns to the depot. For open routes, termination occurs when either all drones have been deployed and exhausted their available time, or all nodes in  $P$  have been

assessed. These variant-adaptive termination conditions ensure solution validity across all PDRA configurations while maintaining consistency with the masking constraints defined in the update phase.

## 5.2. Multi-task training

UM employs policy optimization with multiple optima (POMO) adapted for multi-task learning to simultaneously handle all PDRA variants within a single model (Kwon et al. 2020, Liu et al. 2024, Zhou et al. 2024, Berto et al. 2024). This approach eliminates the computational overhead of training separate models for each variant while leveraging shared knowledge across problem structures.

We implement a batch-wise strategy where each training batch focuses on consistent attribute configurations, ensuring uniform decoder sequence lengths within batches to facilitate efficient parallel processing and stable gradient computation (Liu et al. 2024, Zhou et al. 2024). Attributes are stochastically activated with 50% probability to enhance model robustness across diverse constraint configurations, allowing the model to learn adaptive strategies for both OR and TW scenarios. A critical challenge in multi-task learning is reward discrepancy across attribute combinations; for example, scenarios with TW may yield different reward scales compared to those without. To mitigate training biases, we implement a normalized reward strategy combining exponentially moving average (EMA) with Z-score normalization, following the approach established in Gong et al. (2025). This normalization anchors rewards to their historical trajectories within each attribute regime, enabling stable multi-task convergence across diverse PDRA variants. Algorithm 1 summarizes the complete multi-task training framework. The unified architecture learns shared representations across PDRA variants while adapting to variant-specific constraints through the attention mechanism and masking strategies, achieving superior performance compared to specialized single-task models.

## 6. Finetuning to unseen attributes

The dynamic nature of post-disaster environments demands adaptive models capable of integrating previously unseen attributes without necessitating full retraining. To validate the adaptability and practical deployment flexibility of the proposed UM, we propose a lightweight finetuning mechanism that enables efficient adaptation to emerging PDRA requirements. For this study, the MD attribute is selected as a representative unseen attribute, as it introduces fundamental structural modifications to the routing problem while maintaining compatibility with existing PDRA variants. Thus, MD serves as a representative unseen attribute and is excluded from the initial training phase to simulate the realistic scenario where new operational requirements emerge post-deployment.

**Algorithm 1** Multi-Task POMO Training

---

```

1: Input: Epochs  $E$ , iterations  $T$ , batch size  $B$ , parameter ranges  $\{(p_{\max}, Q, K)\}$ 
2: Initialize: Policy network  $\theta$ 
3: for  $e = 1$  to  $E$  do
4:   for  $t = 1$  to  $T$  do
5:     Generate  $B$  problem instances
6:     Sample a parameter combination  $(p_{\max}, Q, K)$ 
7:     Activate OR, TW attributes with probability 50%
8:     Compute solutions via  $\theta$ -parameterized policy
9:     Normalize rewards using EMA with Z-score normalization
10:    Update  $\theta$  using Adam optimizer via policy gradients
11:  end for
12: end for
13: Return: Optimized parameters  $\theta$ 

```

---

The finetuning mechanism leverages efficient adapter layers, drawing inspiration from recent advancements in parameter-efficient transfer learning (Berto et al. 2024). The core principle involves parameter augmentation with zero-initialized entries; this design choice ensures the preservation of pre-trained knowledge while accommodating new attribute-specific requirements. For integrating a new attribute, the finetuning mechanism requires only minimal modifications to the input embedding and the decoder's context embedding. Taking MD as an example, these modifications are as follows. The original depot node embedding formulation:

$$\mathbf{h}_o^{[0]} = [x_o, y_o, p_{\max}, Q, K, O] \mathbf{W}_o + \mathbf{b}_o, \quad (12)$$

requires extension to handle multiple depots  $D \subseteq N$  where  $|D| \geq 2$ . Rather than modifying the existing learned parameters  $\mathbf{W}_o \in \mathbb{R}^{6 \times d}$  and  $\mathbf{b}_o \in \mathbb{R}^d$ , architectural consistency is maintained by computing each depot's embedding ( $d \in D$ ) using the same projection matrices with depot-specific coordinates  $(x_d, y_d)$ . This design preserves the semantic understanding of depot-related features acquired during pre-training while enabling the representation of multiple depot instances. To incorporate MD-specific state information for effective multi-depot routing decisions, the decoder's context embedding mechanism is enhanced as follows:

$$\mathbf{h}_c^{(t)} = \begin{cases} [\mathbf{h}_i, d_t, k_t, x_d, y_d] \mathbf{W}'_c + \mathbf{b}'_c & t \geq 1, \\ [\mathbf{h}_o, d_t, k_t, x_d, y_d] \mathbf{W}'_c + \mathbf{b}'_c & t = 0. \end{cases} \quad (13)$$

Compared with the original context embedding in Equation (6), the enhanced context embedding in Equation (13) adds two dimensions  $(x_d, y_d)$ . These two additional dimensions serve specific

operational functions, particularly capturing origin depot coordinates to enforce return constraints in closed-route configurations, thereby ensuring spatial awareness for depot-specific return requirements. Correspondingly, the original projection matrices  $\mathbf{W}_c \in \mathbb{R}^{(d+2) \times d}$  and  $\mathbf{b}_c \in \mathbb{R}^d$  are expanded via zero-initialized parameter expansion:

$$\mathbf{W}'_c = \begin{bmatrix} \mathbf{W}_c \\ \mathbf{0}_{2 \times d} \end{bmatrix}; \quad \mathbf{b}'_c = \begin{bmatrix} \mathbf{b}_c \\ \mathbf{0}_{2 \times 1} \end{bmatrix}. \quad (14)$$

The decoder's termination conditions require modification to accommodate multi-depot scenarios. The updated termination criteria are compatible with both OR and MD attributes. For closed routes with MD, termination occurs when all drones have completed their routes and returned to their assigned depots, or when all nodes with damage information values have been visited and the active drone returns to its assigned depot. For open routes with MD, termination occurs when all drones have been deployed and completed their missions, or when all nodes with damage information values have been visited. These modified termination conditions ensure valid solution generation across multi-depot configurations while maintaining compatibility with existing route type constraints. By leveraging the shared knowledge encoded in UM's representations, the fine-tuning process requires significantly fewer training iterations compared to training from scratch, an efficiency critical for rapid deployment in disaster response scenarios where new operational requirements may emerge with limited preparation time.

## 7. Experiments

This section evaluates the proposed unified model through comprehensive experiments across multiple PDRA variants and network scales, examining solution quality, computational efficiency, scalability, and adaptability to unseen attributes.

### 7.1. Experiment setup and benchmarks

The experimental configuration encompasses model architecture specifications, problem parameter settings, training infrastructure, and benchmark methods.

**Model Parameters.** UM employs an embedding size  $d = 128$  and features a modern transformer encoder consisting of  $l = 6$  layers with 8-head attention and SGLUFFN with a hidden size of 512. These architectural settings are informed by successful applications in neural combinatorial optimization (Kool et al. 2018, Kwon et al. 2020, Luo et al. 2023, Zhou et al. 2024, Liu et al. 2024, Berto et al. 2024, Gong et al. 2025). UM configuration yields approximately 1.3 million trainable parameters. Training spans 200 epochs (batch size = 64) on 100,000 on-the-fly generated instances to ensure robust learning across diverse problem variants. The Adam optimizer employs an initial learning rate of  $10^{-4}$ ,  $L_2$  regularization ( $10^{-6}$  weight decay), and learning rate decay ( $\times 0.1$  at epochs 175 and 195, respectively).

**Problem Parameters.** UM is trained on 100-node instances, comprising 50 nodes in set  $P$  (with damage information values, representing 50 assessable road links) and 50 nodes in set  $N$  (without damage information, including one depot). To evaluate generalization capability, testing is conducted on larger instances (200, 400, 600, 800, and 1,000 nodes), each with 50% nodes in  $P$  and 50% in  $N$ . Damage information values for  $P$  are uniformly sampled from [1, 10] and normalized by division by 10. Practically, drones have a 2-hour battery flight time limit  $Q$  and a speed of 60 km/h (Zhang et al. 2023). Given the time-critical nature of disaster response, assessment time limits  $p_{\max}$  are set to 30, 45, and 60 minutes (corresponding to 30, 45, and 60 km flight distances, respectively). Since  $Q$  is significantly larger than  $p_{\max}$ ,  $Q$  is not considered in subsequent experiments, with a focus on  $p_{\max}$ . Road network coordinates are normalized to [0, 1], with link lengths scaled accordingly. For simplified data generation, training uses  $p_{\max} = 2, 3, 4$  corresponding to 30, 45, and 60 minutes in real-world distances. For parameter  $K$ , training uses 2, 3, or 4 drones. For the latest time windows parameter  $l_i$  in the TW attribute, the generation method adopted is consistent with the approach proposed for classical vehicle routing problems in the existing literature (Zhao et al. 2020, Liu et al. 2024, Zhou et al. 2024, Berto et al. 2024).

**Training Infrastructure.** Training is conducted on Google Colab (<https://colab.research.google.com>) using an NVIDIA A100 GPU. Each epoch requires approximately 7.2 minutes, resulting in a total training duration of around 24 hours for 200 epochs.

**Benchmarks.** For comparison, two benchmarks are established to evaluate the approach as listed below:

- Traditional Optimization Baseline: The mathematical model corresponding to each PDRA variant is detailed in Appendix 8, and each variant can thus be solved using commercial optimization solvers (e.g., Gurobi). Like UM, this approach requires no domain knowledge for algorithm design but necessitates separate model formulations and solving procedures for each of the 8 variants, highlighting the computational overhead UM aims to eliminate. Gurobi is evaluated with multiple time limits (60s, 10×60s, 20×60s, 30×60s) to reflect different urgency levels in disaster response scenarios.
- Single-Task Deep Learning Baseline: Comparisons are made with single-task DRL methods from the literature, specifically the AEDM proposed by Gong et al. (2025). These include:
  - AEDM-Basic: Single-task model for PDRA-Basic
  - AEDM-OR: Single-task model for PDRA-OR
  - AEDM-TW: Single-task model for PDRA-TW
  - AEDM-OR-TW: Single-task model for PDRA-OR-TW
  - AEDM-MD: Single-task model for PDRA-MD
  - AEDM-OR-MD: Single-task model for PDRA-OR-MD

**Table 3 Comparison of Methodological Efficiencies**

Method	No. of models	Total Parameters (M)	Total Epochs	Training Cost (h)
Existing literature	8	10.4	1,600	192
Ours	1	1.3	200	24

- AEDM-TW-MD: Single-task model for PDRA-TW-MD
- AEDM-OR-TW-MD: Single-task model for PDRA-OR-TW-MD.

Each baseline requires separate training for specific problem variants, necessitating multiple models for comprehensive coverage. In contrast, UM handles all 8 variants within a single model. As shown in Table 3, the existing literature approach requires training 8 separate models (one for each variant) with a total of 10.4 million parameters across 1,600 epochs, resulting in 192 hours of training time. UM achieves comprehensive coverage with a single 1.3 million parameter model trained for 200 epochs in just 24 hours, representing an 8 $\times$  reduction in model count, parameter count, training epochs, and training time.

Since post-disaster response requires assessing road networks at multiple affected locations (e.g., after earthquakes or floods), the task is inherently multi-instance rather than single-instance. Therefore, Gurobi, AEDM, and the proposed UM must all be evaluated on their ability to handle multiple instances efficiently, making both solution quality and computational speed equally critical. For this reason, the following results are averaged over 10 randomly generated problem instances. For the single-task AEDM and UM, we report the total computation time across the 10 instances, while for Gurobi we report the average time per instance, which places Gurobi in a relatively favorable position.

## 7.2. Computational performance

Tables 4 and 5 present the numerical experiments of the comparisons for 200-node and 400-node networks, where the column of gap is calculated as  $\text{Gap} = (y - y_{\text{other}})/y$ , where  $y$  denotes the objective value of UM and  $y_{\text{other}}$  that of the comparison method. From these results, two key insights emerge:

- Solution Quality Superiority.** UM consistently achieves the highest objective values across all PDRA variants. For the traditional commercial solver (Gurobi), solution quality gradually improves as the time limit extends; however, even with the longest time limit (30 $\times$ 60s, 30 minutes), its final solution quality remains suboptimal compared to UM. In 400-node networks, Gurobi frequently fails to generate feasible solutions within practical time limits (marked by  $\times$  in Table 5). For single-task AEDMs, high solution quality is only achieved when the model is specifically trained for the target PDRA variant. If a single-task AEDM is applied to a non-matching variant (e.g., using AEDM-Basic for PDRA-OR-TW), its solution quality drops significantly.

**Table 4 Performance Comparison of Methods in 200-Node Network ( $p_{\max} = 30$  min, Varying Drone Fleet sizes)**

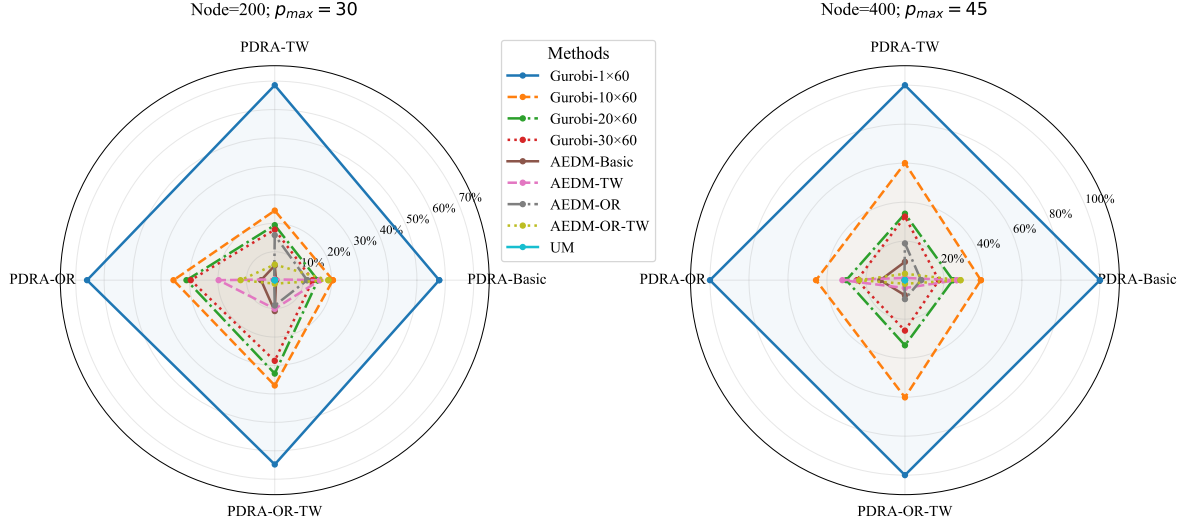
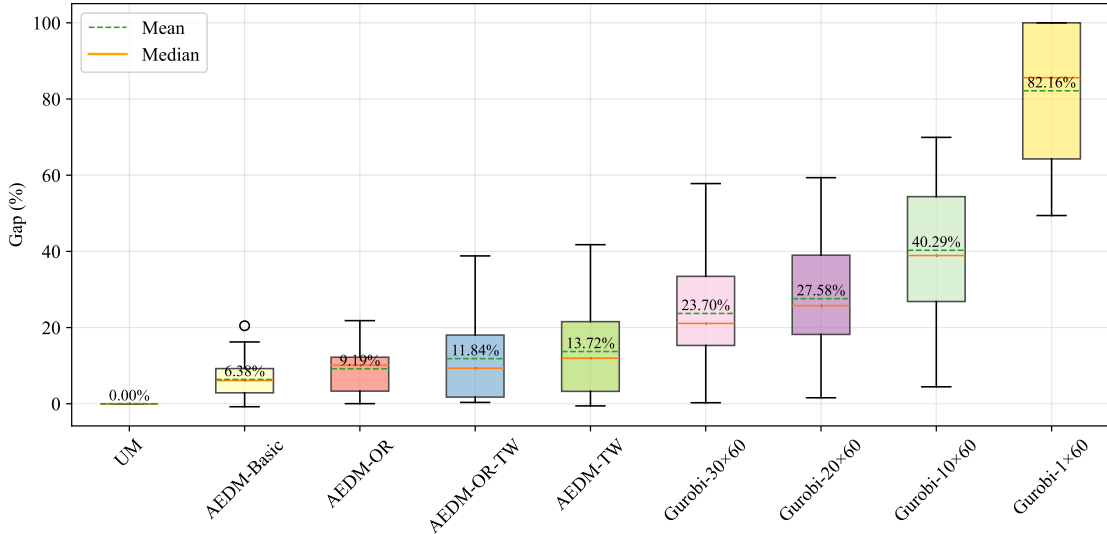
Type	Method	#Drone	Time (s)	Value	Gap	#Drone	Time (s)	Value	Gap
PDRA-Basic	Gurobi	2	60	8.18	49.41%	3	60	9.66	56.23%
			10×60	15.45	4.45%		10×60	16.49	25.28%
			20×60	15.68	3.03%		20×60	20.83	5.62%
			30×60	16.11	0.37%		30×60	21.04	4.67%
	AEDM-Basic	2	1	16.28	-0.68%	3	1	21.98	0.41%
	AEDM-OR	1	1	14.47	10.51%	1	1	19.61	11.15%
	AEDM-TW	1	1	14.18	12.31%	1	1	18.95	14.14%
	AEDM-OR-TW	1	1	14.07	12.99%	1	1	18.12	17.90%
	UM	1	1	16.17	0.00%	1	1	22.07	0.00%
	Gurobi	4	60	9.89	63.14%	60	11.67	62.60%	
PDRA-OR	Gurobi	2	10×60	20.08	25.16%	5	10×60	22.80	26.92%
			20×60	20.08	25.16%		20×60	22.80	26.92%
			30×60	20.78	22.55%		30×60	23.15	25.80%
	AEDM-Basic	2	2	26.59	0.89%		2	30.80	1.28%
	AEDM-OR	2	2	23.59	12.08%	2	2	27.51	11.83%
	AEDM-TW	2	2	22.55	15.95%	2	2	24.67	20.93%
	AEDM-OR-TW	2	2	21.75	18.93%	2	2	23.21	25.61%
	UM	2	2	26.83	0.00%	2	2	31.20	0.00%
	Gurobi	4	60	9.89	70.70%	60	11.33	71.19%	
	Gurobi	6	10×60	20.08	40.52%	10×60	22.80	42.03%	
PDRA-TW	Gurobi	2	20×60	20.08	40.52%	5	20×60	22.80	42.03%
			30×60	20.90	38.09%		30×60	23.60	39.99%
	AEDM-Basic	2	2	32.14	4.80%		2	37.52	4.60%
	AEDM-OR	2	2	33.72	0.12%	2	2	39.32	0.03%
	AEDM-TW	2	2	25.85	23.43%	2	2	28.56	27.38%
	AEDM-OR-TW	2	2	27.54	18.42%	2	2	35.51	9.71%
	UM	2	2	33.76	0.00%	2	2	39.33	0.00%
	Gurobi	4	60	4.28	70.11%	60	5.83	69.99%	
	Gurobi	8	10×60	10.51	26.61%	10×60	16.57	14.72%	
PDRA-OR-TW	Gurobi	2	20×60	11.86	17.18%	3	20×60	16.57	14.72%
			30×60	12.10	15.50%		30×60	16.57	14.72%
	AEDM-Basic	2	2	13.59	5.10%		2	18.77	3.40%
	AEDM-OR	2	2	12.40	13.41%	2	2	16.98	12.61%
	AEDM-TW	2	2	14.40	-0.56%	2	2	19.34	0.46%
	AEDM-OR-TW	2	2	14.22	0.70%	2	2	18.47	4.94%
	UM	2	2	14.32	0.00%	2	2	19.43	0.00%
	Gurobi	4	60	7.02	70.76%	60	10.22	63.43%	
	Gurobi	8	10×60	18.17	24.32%	10×60	18.92	32.28%	
PDRA-OR-TW	Gurobi	2	20×60	19.41	19.16%	5	20×60	20.58	26.34%
			30×60	19.41	19.16%		30×60	21.86	21.76%
	AEDM-Basic	2	2	22.78	5.12%		2	25.99	6.98%
	AEDM-OR	2	2	19.62	18.28%	2	2	22.62	19.04%
	AEDM-TW	2	2	23.98	0.12%	2	2	27.64	1.07%
	AEDM-OR-TW	2	2	22.98	4.29%	2	2	24.56	12.10%
	UM	2	2	24.01	0.00%	2	2	27.94	0.00%
	Gurobi	4	60	6.10	64.09%	60	7.64	67.48%	
	Gurobi	8	10×60	10.51	38.10%	10×60	16.57	29.46%	
PDRA-OR-TW	Gurobi	2	20×60	11.86	30.15%	3	20×60	16.57	29.46%
			30×60	14.26	16.02%		30×60	16.57	29.46%
	AEDM-Basic	2	2	15.11	11.01%		2	20.86	11.20%
	AEDM-OR	2	2	15.74	7.30%	2	2	21.36	9.07%
	AEDM-TW	2	2	15.51	8.66%	2	2	21.20	9.75%
	AEDM-OR-TW	2	2	16.76	1.30%	2	2	23.10	1.66%
	UM	2	2	16.98	0.00%	2	2	23.49	0.00%
	Gurobi	4	60	9.68	66.52%	60	13.09	61.17%	
	Gurobi	8	10×60	18.29	36.76%	10×60	18.92	43.85%	
PDRA-OR-TW	Gurobi	2	20×60	19.41	32.88%	5	20×60	20.58	38.93%
			30×60	19.41	32.88%		30×60	21.86	35.13%
	AEDM-Basic	2	2	26.02	10.03%		2	29.92	11.22%
	AEDM-OR	2	2	26.38	8.78%	2	2	30.15	10.53%
	AEDM-TW	2	2	25.94	10.30%	2	2	29.79	11.60%
	AEDM-OR-TW	2	2	28.57	1.21%	2	2	33.45	0.74%
	UM	2	2	28.92	0.00%	2	2	33.70	0.00%

b) **Computational Efficiency.** UM delivers real-time performance, generating valid solutions within 1–2 seconds across all tested network scales and drone fleet sizes. In contrast, Gurobi requires 10–30 minutes to reach reasonable-quality solutions, far exceeding the time-critical

**Table 5 Performance Comparison of Methods in 400-Node Network ( $p_{\max} = 45$  min, Varying Drone Fleet sizes)**

Type	Method	#Drone	Time (s)	Value	Gap	#Drone	Time (s)	Value	Gap
PDRA-Basic	Gurobi	2	60	x	100%	3	60	x	100%
			10×60	28.07	24.83%		10×60	37.30	27.83%
			20×60	32.64	12.59%		20×60	46.52	9.98%
			30×60	33.98	9.00%		30×60	46.89	9.27%
	AEDM-Basic	1		37.63	-0.78%		1	51.34	0.66%
	AEDM-OR	1		35.77	4.20%		1	46.54	9.95%
	AEDM-TW	1		31.87	14.65%		1	38.31	25.87%
	AEDM-OR-TW	1		31.25	16.31%		1	37.15	28.12%
	UM	1		37.34	0.00%		1	51.68	0.00%
	Gurobi	4	60	x	100%	5	60	x	100%
			10×60	29.19	54.20%		10×60	37.17	48.91%
			20×60	40.48	36.49%		20×60	44.23	39.21%
	AEDM-Basic	1		59.99	20.00%		1	49.93	31.38%
	AEDM-OR	1		64.16	-0.66%		1	72.42	0.47%
	AEDM-TW	1		58.21	8.68%		1	65.28	10.28%
	AEDM-OR-TW	1		44.35	30.42%		1	47.23	35.09%
	UM	1		42.47	33.37%		1	46.43	36.19%
	PDRA-OR	2	60	x	100%		60	x	100%
			10×60	28.07	32.46%		10×60	37.30	35.25%
			20×60	32.64	21.46%		20×60	46.52	19.25%
	AEDM-Basic	1		34.29	17.49%		1	47.84	16.96%
	AEDM-OR	1		39.61	4.69%		1	45.81	20.48%
	AEDM-TW	1		41.28	0.67%		1	57.57	0.07%
	AEDM-OR-TW	1		33.81	18.65%		1	40.46	29.77%
	UM	1		35.48	14.63%		1	50.54	12.27%
	Gurobi	4	60	x	100%	1	60	x	100%
			10×60	29.19	59.89%		10×60	37.17	54.87%
			20×60	48.40	33.49%		20×60	44.23	46.30%
	AEDM-Basic	1		52.97	27.21%		1	51.94	36.94%
	AEDM-OR	1		60.97	16.22%		1	74.83	9.14%
	AEDM-TW	1		72.55	0.30%		1	82.27	0.11%
	AEDM-OR-TW	1		45.01	38.15%		1	47.97	41.76%
	UM	1		52.28	28.16%		1	50.40	38.81%
	PDRA-TW	2	60	x	100%	1	60	x	100%
			10×60	10.18	60.97%		10×60	19.91	44.43%
			20×60	25.67	1.57%		20×60	28.26	21.13%
	AEDM-Basic	1		26.01	0.27%		1	28.52	20.40%
	AEDM-OR	1		23.23	10.93%		1	32.42	9.52%
	AEDM-TW	1		22.27	14.61%		1	28.87	19.43%
	AEDM-OR-TW	1		26.03	0.19%		1	35.86	-0.08%
	UM	1		25.99	0.35%		1	34.51	3.68%
	Gurobi	4	60	x	100%	1	60	x	100%
			10×60	10.18	65.19%		10×60	15.28	69.67%
			20×60	15.20	59.15%		20×60	22.91	54.53%
	AEDM-Basic	1		18.43	57.80%		1	24.21	51.93%
	AEDM-OR	1		39.90	8.63%		1	46.07	8.54%
	AEDM-TW	1		34.14	21.82%		1	40.47	19.65%
	AEDM-OR-TW	1		42.16	3.46%		1	49.80	1.13%
	UM	1		41.38	5.24%		1	48.37	3.97%
	PDRA-OR-TW	2	60	x	100%	1	60	x	100%
			10×60	10.18	61.25%		10×60	19.91	43.77%
			20×60	25.66	2.32%		20×60	28.26	20.19%
	AEDM-Basic	1		26.02	0.95%		1	32.11	9.32%
	AEDM-OR	1		24.11	8.22%		1	33.02	6.75%
	AEDM-TW	1		23.79	9.44%		1	31.69	10.51%
	AEDM-OR-TW	1		25.58	2.63%		1	33.70	4.83%
	UM	1		26.10	0.65%		1	34.92	1.38%
	Gurobi	4	60	x	100%	1	60	x	100%
			10×60	10.18	65.54%		10×60	15.28	69.93%
			20×60	17.93	59.35%		20×60	24.50	51.79%
	AEDM-Basic	1		25.29	42.67%		1	25.14	50.53%
	AEDM-OR	1		40.37	8.48%		1	46.98	7.56%
	AEDM-TW	1		39.55	10.34%		1	46.46	8.58%
	AEDM-OR-TW	1		42.00	4.78%		1	48.84	3.90%
	UM	1		43.33	1.77%		1	49.00	3.58%
	AEDM-Basic	2	60	x	100%	1	60	x	100%
			10×60	10.18	66.67%		10×60	15.28	70.00%
			20×60	25.66	2.32%		20×60	28.26	20.19%
	AEDM-OR	1		26.02	0.95%		1	32.11	9.32%
	AEDM-TW	1		24.11	8.22%		1	33.02	6.75%
	AEDM-OR-TW	1		23.79	9.44%		1	31.69	10.51%
	UM	1		25.58	2.63%		1	33.70	4.83%
	AEDM-Basic	4	60	x	100%	1	60	x	100%
			10×60	10.18	67.73%		10×60	15.28	70.00%
			20×60	25.66	2.32%		20×60	28.26	20.19%
	AEDM-OR	1		26.02	0.95%		1	32.11	9.32%
	AEDM-TW	1		24.11	8.22%		1	33.02	6.75%
	AEDM-OR-TW	1		23.79	9.44%		1	31.69	10.51%
	UM	1		25.58	2.63%		1	33.70	4.83%

demands of post-disaster response. Single-task AEDMs also suffer from inefficiency. They require separate models (one for each PDRA variant), leading to an increase in total train-

**Figure 4** Average Performance Gap Calculation**Figure 5** UM vs. Baseline Methods: Average Gap Computation

ing time and necessitating variant-specific deployment, which further complicates real-world application.

Figures 4 and 5 visually corroborate these findings. The radar charts in Figure 4 show UM consistently occupying the outermost (best) performance positions across all parameter settings and problem variants, indicating superior and stable performance under diverse operational constraints. Figure 5 shows that UM consistently outperforms baseline methods in terms of solution quality (total collected information value). Specifically, UM surpasses the best single-task model by 6%–14% and Gurobi by 24%–82% across tested configurations.

### 7.3. Sensitivity analysis

To evaluate the robustness and scalability of the proposed UM, this section conducts sensitivity analyses across three critical dimensions: drone fleet sizes, maximum allowable assessment time constraints, and network scales. These analyses assess performance stability when key parameters deviate from training conditions, demonstrating the model's applicability to diverse post-disaster scenarios. All sensitivity tests are conducted on the PDRA-OR-TW variant, which simultaneously incorporates the open route and time window constraints, thereby representing a complex and practically relevant scenario. The results yield three key insights:

- a) Table 6 shows performance sensitivity to varying drone fleet sizes (4, 5, 6, and 7 drones) on a fixed 400-node network with  $p_{max} = 45$  minutes. This analysis is particularly critical for disaster response scenarios, where drone availability often fluctuates due to uncertainties. Table 6 reveals that UM maintains consistent superiority across varying drone fleet sizes, with performance gaps ranging from 1.20% to 10.34% over the single-task AEDM baselines. Gurobi fails to produce feasible solutions within 60 seconds for all fleet configurations, highlighting UM's advantage in time-critical scenarios. The computational time scales linearly with fleet size (2–4 seconds), demonstrating efficient parallelization capabilities essential for large-scale disaster response operations.
- b) Table 7 shows performance under varying maximum allowable assessment times (20, 30, 40, and 50 minutes) with fixed network scale (400 nodes) and drone fleet size (4). This analysis simulates the time-critical nature of disaster response operations where assessment windows may vary based on emergency severity and resource availability. The results demonstrate UM's robustness under temporal constraints, maintaining superior performance across all maximum allowable assessment time constraints with gaps ranging from -0.20% to 16.07% over single-task AEDM baselines. Gurobi consistently fails at 60-second limits across all time windows, requiring 10–30 minutes to achieve suboptimal solutions.
- c) Table 8 shows UM's scalability across varying network scales (400, 600, 800, and 1,000 nodes) while maintaining fixed assessment time ( $p_{max} = 45$  minutes) and drone fleet size (4). The results reveal strong scalability characteristics, with UM preserving solution quality superiority across all tested network scales. Performance gaps over the single-task AEDM baselines range from 0.17% to 11.65%, while its computational time remains within real-time limits (2–10 seconds). In contrast, Gurobi fails completely on networks larger than 400 nodes, even with extended time limits up to 30×60 seconds, underscoring UM's practical advantage for large-scale PDRA applications where traditional optimization methods become computationally intractable.

**Table 6 Sensitivity analysis under varying drone fleet sizes (400 nodes,  $p_{\max} = 45$ )**

Method	Drone fleet sizes											
	4			5			6			7		
	Value	Gap	Time (s)	Value	Gap	Time (s)	Value	Gap	Time (s)	Value	Gap	Time (s)
Gurobi	<b>X</b>	100%	60	<b>X</b>	100%	60	<b>X</b>	100%	60	<b>X</b>	100%	60
	15.20	65.54%	10×60	15.28	69.93%	10×60	18.92	66.13%	10×60	21.56	63.66%	10×60
	17.93	59.35%	20×60	24.50	51.79%	20×60	28.65	48.71%	20×60	30.89	47.93%	20×60
	25.29	42.67%	30×60	25.14	50.53%	30×60	32.76	41.35%	30×60	34.09	42.54%	30×60
AEDM-Basic	40.37	8.48%	2	46.98	7.56%	2	50.28	9.99%	3	53.91	9.14%	4
AEDM-OR	39.55	10.34%	2	46.46	8.58%	2	50.20	10.13%	3	53.41	9.98%	4
AEDM-TW	42.00	4.78%	2	48.84	3.90%	2	52.37	6.25%	3	56.07	5.49%	4
AEDM-OR-TW	43.33	1.77%	2	49.00	3.58%	2	55.19	1.20%	3	58.57	1.28%	4
UM	44.11	0.00%	2	50.82	0.00%	2	55.86	0.00%	3	59.33	0.00%	4

**Table 7 Sensitivity analysis under varying maximum allowable assessment times ( $p_{\max}$ ) (400 nodes, 4 drones)**

Method	Maximum allowable assessment times											
	20			30			40			50		
	Value	Gap	Time (s)	Value	Gap	Time (s)	Value	Gap	Time (s)	Value	Gap	Time (s)
Gurobi	<b>X</b>	100%	60	<b>X</b>	100%	60	<b>X</b>	100%	60	<b>X</b>	100%	60
	7.02	43.02%	10×60	10.04	60.81%	10×60	14.89	61.47%	10×60	12.95	74.24%	10×60
	8.21	33.36%	20×60	12.85	49.84%	20×60	18.02	53.38%	20×60	23.90	52.47%	20×60
	8.25	33.04%	30×60	15.22	40.59%	30×60	22.40	42.04%	30×60	28.79	42.74%	30×60
AEDM-Basic	11.91	3.33%	1	23.73	7.38%	2	34.47	10.82%	2	42.20	16.07%	2
AEDM-OR	11.93	3.17%	1	21.82	14.83%	2	34.62	10.43%	2	43.33	13.82%	2
AEDM-TW	11.89	3.49%	1	22.59	11.83%	2	34.44	10.89%	2	44.37	11.75%	2
AEDM-OR-TW	12.34	-0.16%	1	25.67	-0.20%	2	37.84	2.10%	2	49.14	2.27%	2
UM	12.32	0.00%	1	25.62	0.00%	2	38.65	0.00%	2	50.28	0.00%	2

**Table 8 Sensitivity analysis under varying network scales ( $p_{\max} = 45$ , 4 drones)**

Method	Network scales											
	400			600			800			1000		
	Value	Gap	Time (s)	Value	Gap	Time (s)	Value	Gap	Time (s)	Value	Gap	Time (s)
Gurobi	<b>X</b>	100%	60	<b>X</b>	100%	60	<b>X</b>	100%	60	<b>X</b>	100%	60
	15.20	65.54%	10×60	<b>X</b>	100%	10×60	<b>X</b>	100%	10×60	<b>X</b>	100%	10×60
	17.93	59.35%	20×60	<b>X</b>	100%	20×60	<b>X</b>	100%	20×60	<b>X</b>	100%	20×60
	25.29	42.67%	30×60	<b>X</b>	100%	30×60	<b>X</b>	100%	30×60	<b>X</b>	100%	30×60
AEDM-Basic	40.37	8.48%	2	43.06	10.23%	4	47.24	9.31%	8	49.91	11.57%	10
AEDM-OR	39.55	10.34%	2	42.38	11.65%	4	46.22	11.27%	8	50.53	10.48%	10
AEDM-TW	42.00	4.78%	2	45.34	5.49%	4	49.00	5.94%	8	53.17	5.80%	10
AEDM-OR-TW	43.33	1.77%	2	47.89	0.17%	4	51.66	0.83%	8	55.83	1.08%	10
UM	44.11	0.00%	2	47.97	0.00%	4	52.09	0.00%	8	56.44	0.00%	10

The sensitivity analyses collectively validate UM's robustness across critical operational parameters, confirming its suitability for deployment in diverse post-disaster environments where parameter variations are inevitable. The consistent performance superiority and computational efficiency across all tested dimensions demonstrate the model's practical reliability for time-sensitive emergency response operations where both solution quality and computational speed are important.

#### 7.4. Real-world application

To further validate the practical applicability of the proposed UM in real-world post-disaster scenarios, experiments are conducted on the publicly available Anaheim transporta-

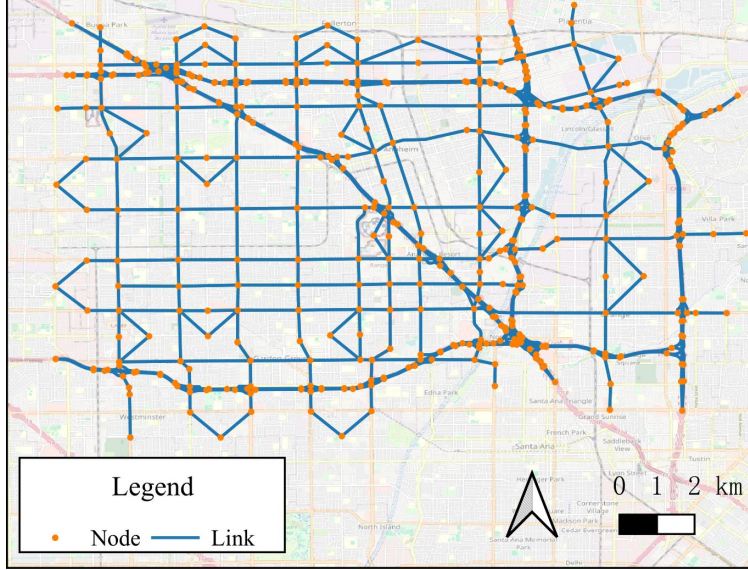


**Figure 6** Anaheim Network

tion network (as shown in Figure 6), with data sourced from <https://github.com/bstabler/TransportationNetworks>. This network simulates the complexity of a metropolitan road system, which is typical of large-scale PDRAAs. The original network (416 nodes and 914 links) is transformed into a 1330-node structure (including 914 artificial nodes for road links) using the transformation method detailed in Section 3.2. The experimental setup includes 7 drones, and the maximum assessment time  $p_{max}$  is set to 45 minutes. Three benchmark approaches are used: UM, single-task AEDMs (Gong et al. 2025), and Gurobi. In the experiments, UM solves these 4 PDRA variants in a unified manner, while the four single-task AEDMs solve all variants (with reported results being their average values); additionally, Gurobi’s time limit is extended to 10,000 seconds to account for the increased problem complexity. Results in Figure 7 show that UM consistently outperforms the other two benchmarks: compared with the single-task AEDMs, it achieves an average performance improvement of 7.9% (ranging from 7.2% to 8.4%) by leveraging multi-task knowledge sharing, and relative to Gurobi, it yields a 25.5% improvement (ranging from 23.6% to 27.8%). In terms of efficiency, UM only takes approximately 10 seconds to solve the problem, while the single-task AEDMs require variant-specific deployment; Gurobi’s 10,000-second runtime, meanwhile, is entirely impractical for real-world use. These findings confirm UM’s scalability and robustness under realistic network complexity, as well as its flexibility for rapid deployment in time-critical PDRA applications.

## 7.5. Finetuning

To evaluate the proposed lightweight finetuning mechanism for incorporating previously unseen attributes, experiments are conducted on 400-node networks with 2 depots, each deploying 3

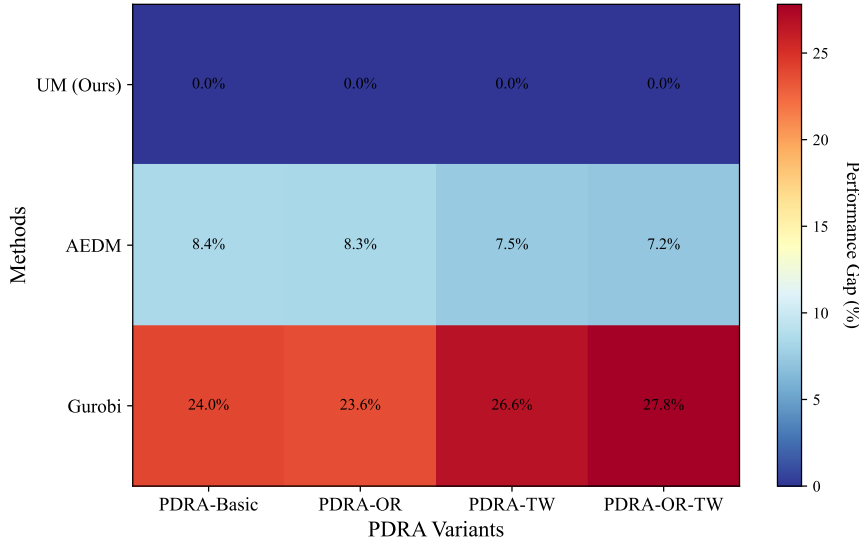


**Figure 7 Performance Gap Comparison of UM, AEDM, and Gurobi Across Four PDRA Variants on the Anaheim Network**

**Table 9 Performance Comparison of Methods for MD-Integrated PDRA Variants**

Method	AEDM-MD			AEDM-OR-MD			AEDM-TW-MD			AEDM-OR-TW-MD		
	Value	Gap	Time (s)	Value	Gap	Time (s)	Value	Gap	Time	Value	Gap	Time (s)
Gurobi	<b>x</b>	100%	60	<b>x</b>	100%	60	<b>x</b>	100%	60	<b>x</b>	100%	60
	38.42	46.05%	10*60	41.22	51.07%	10*60	31.06	39.35%	10*60	38.12	39.15%	10*60
	48.69	31.62%	20*60	55.12	34.58%	20*60	40.82	20.29%	20*60	47.51	24.17%	20*60
	53.24	25.24%	30*60	61.84	26.60%	30*60	41.45	19.06%	30*60	52.16	16.74%	30*60
AEDM-MD	70.25	1.35%	3	69.55	17.45%	3	39.47	22.93%	4	50.85	18.83%	4
AEDM-OR-MD	59.19	16.88%	3	83.03	1.45%	3	42.52	16.97%	4	51.87	17.21%	4
AEDM-TW-MD	57.38	19.42%	3	62.58	25.72%	3	49.68	2.99%	4	53.25	15.00%	4
AEDM-OR-TW-MD	55.83	21.60%	3	66.25	21.36%	3	41.41	19.14%	4	60.53	3.38%	4
UM-Zero-Shot	57.92	18.66%	3	66.48	21.09%	3	39.54	22.79%	4	52.25	16.60%	4
UM-10-Epochs	71.21	0.00%	3	84.25	0.00%	3	51.21	0.00%	4	62.65	0.00%	4

drones under a maximum assessment time constraint of  $p_{max} = 45$  minutes. The MD attribute, deliberately excluded from initial UM training, serves as the representative unseen attribute to assess adaptation capabilities. The finetuning mechanism leverages efficient adapter layers through parameter augmentation with zero-initialized entries, requiring only minimal modifications to the input embedding and decoder’s context embedding while preserving the valuable multi-task knowledge encoded in the original parameters. Four approaches are systematically compared: (i) Gurobi, representing traditional optimization; (ii) single-task AEDM variants (AEDM-MD, AEDM-OR-MD, AEDM-TW-MD, and AEDM-OR-TW-MD), each trained from scratch for 200 epochs; (iii) UM-Zero-Shot, where the pre-trained UM is directly applied to MD problems without adaptation; and (iv) UM-10-Epochs, which applies the lightweight adapter mechanism with only 10 epochs of finetuning. The results are summarized in Table 9.

Compared with Gurobi, UM-10-Epochs shows advantages in both solution quality and efficiency. Gurobi often fails to produce feasible solutions within the 60-second limit and requires 10–30 min-

utes to obtain suboptimal outcomes, whereas UM-10-Epochs consistently generates high-quality solutions in just a few seconds. This indicates that the adapter mechanism effectively integrates the unseen MD attribute without compromising real-time performance, which is essential in post-disaster contexts. When compared with single-task AEDM variants, UM-10-Epochs achieves higher solution quality despite AEDMs undergoing full training on each MD-integrated problem. This highlights that multi-task knowledge transfer, coupled with lightweight finetuning, allows UM to learn new attribute-specific knowledge at only a fraction of the training cost, avoiding the inefficiency of maintaining multiple specialized models. Relative to UM-Zero-Shot, UM-10-Epochs eliminates the moderate performance gap that arises when the MD attribute is directly introduced without adaptation. The short 10-epoch finetuning is sufficient to fully close this gap, yielding optimal performance across all MD-integrated PDRA variants. Overall, these results confirm that even minimal finetuning enables UM to reconcile pre-trained knowledge with new operational constraints, validating the effectiveness of the adapter mechanism. UM thus proves particularly valuable for rapid adaptation in evolving disaster response scenarios, where new operational requirements may emerge with limited preparation time.

## 8. Conclusion

This study addresses the critical challenge of efficient drone routing for PDRA, where existing methods suffer from computational inefficiencies and lack adaptability to diverse operational scenarios. Traditional approaches, including exact optimization methods and single-task deep learning models, require separate solutions for each PDRA variant, resulting in substantial computational overhead and deployment complexity. We propose a UM that consolidates all PDRA variants within a single model through multi-task learning. UM employs a modern transformer architecture incorporating RMS normalization, pre-normalization configuration, FA, and SGLUFFN to enhance computational efficiency and solution quality. The unified approach eliminates the need for variant-specific models while leveraging shared knowledge across different operational constraints. Experimental evaluation demonstrates substantial improvements over existing approaches. UM achieves an 8-fold reduction in training time (24 vs. 192 hours) and model parameters (1.3M vs. 10.4M) compared to training separate models for each variant. Solution quality consistently surpasses single-task methods by 6–14% and traditional optimization approaches by 24–82%, while maintaining real-time performance (1–10 seconds) regardless of network scale or operational complexity. Sensitivity analyses confirm robust performance across varying drone fleet sizes, assessment time constraints, and network scales up to 1,000 nodes. The lightweight adapter mechanism enables efficient incorporation of previously unseen attributes through minimal parameter augmentation and brief finetuning, demonstrating practical adaptability to evolving disaster response requirements.

Future research can proceed in several directions. First, inspired by the scaling laws observed in LLM, where performance improves as parameter size grows (Achiam et al. 2023, Touvron et al. 2023, Guo et al. 2025), we plan to investigate whether increasing the parameter scale of UM (from millions to potentially billions) can yield further gains in solution quality, generalization, and adaptability. Second, beyond PDRA, the unified multi-task learning framework could be applied to broader classes of neural combinatorial optimization problems in emergency logistics, transportation planning, and other time-critical domains, contributing to the development of general-purpose decision-making models for complex real-world systems.

## References

Abuali, T.M., Ahmed, A.A., 2025. Innovative applications of swarm drones in disaster management and rescue operations. *The Open European Journal of Engineering and Scientific Research* , 23–31.

Achiam, J., Adler, S., Agarwal, S., Ahmad, L., Akkaya, I., Aleman, F.L., Almeida, D., Altenschmidt, J., Altman, S., Anadkat, S., et al., 2023. GPT-4 technical report. arXiv preprint arXiv:2303.08774 .

Adsanver, B., Coban, E., Balcik, B., 2025. A predictive multistage postdisaster damage assessment framework for drone routing. *International Transactions in Operational Research* 32, 626–668.

Arii, M., 2013. Rapid assessment in disasters. *Japan Medical Association Journal* 56, 19–24.

Avishan, F., Elyasi, M., Yanikoğlu, İ., Ekici, A., Özener, O.Ö., 2023. Humanitarian relief distribution problem: An adjustable robust optimization approach. *Transportation Science* 57, 1096–1114.

Bello, I., Pham, H., Le, Q.V., Norouzi, M., Bengio, S., 2016. Neural combinatorial optimization with reinforcement learning. arXiv preprint arXiv:1611.09940 .

Berto, F., Hua, C., Zepeda, N.G., Hottung, A., Wouda, N., Lan, L., Park, J., Tierney, K., 2024. Routefinder: Towards foundation models for vehicle routing problem. arXiv preprint arXiv:2406.15007 .

Bravo, R.Z.B., Leiras, A., Cyrino Oliveira, F.L., 2019. The use of uavs in humanitarian relief: An application of pomdp-based methodology for finding victims. *Production and Operations Management* 28, 421–440.

Dao, T., 2023. Flashattention-2: Faster attention with better parallelism and work partitioning. arXiv preprint arXiv:2307.08691 .

Dao, T., Fu, D., Ermon, S., Rudra, A., Ré, C., 2022. FlashAttention: Fast and memory-efficient exact attention with IO-awareness, in: *Proceedings of the 36th International Conference on Neural Information Processing Systems*, pp. 16344–16359.

Dauphin, Y.N., Fan, A., Auli, M., Grangier, D., 2017. Language modeling with gated convolutional networks, in: *Proceedings of the 34th International Conference on Machine Learning*, PMLR. pp. 933–941.

Dubey, A., Jauhri, A., Pandey, A., Kadian, A., Al-Dahle, A., Letman, A., Mathur, A., Schelten, A., Yang, A., Fan, A., et al., 2024. The llama 3 herd of models. arXiv e-prints , arXiv–2407.

Enayati, S., Li, H., Campbell, J.F., Pan, D., 2023. Multimodal vaccine distribution network design with drones. *Transportation Science* 57, 1069–1095.

Ezequiel, C., Cua, M., Libatique, N., Tangonan, G., Honrado, J., Favila, C., Novilla, J., Ilaga, E., Alampay, R., Canos, V., et al., 2015. Aerial imaging consortium: augmenting ground observation with uas remote sensing for environmental resource management. *Journal of the Philippine Geosciences and Remote Sensing Society* 1, 12–20.

Glock, K., Meyer, A., 2020. Mission planning for emergency rapid mapping with drones. *Transportation Science* 54, 534–560.

Gong, H., Sheu, J.B., Wang, Z., Yang, X., Yan, R., 2025. Deep reinforcement learning for real-time drone routing in post-disaster road assessment without domain knowledge. arXiv preprint arXiv:2509.01886. URL: <https://arxiv.org/abs/2509.01886>.

Guo, D., Yang, D., Zhang, H., Song, J., Zhang, R., Xu, R., Zhu, Q., Ma, S., Wang, P., Bi, X., et al., 2025. DeepSeek-R1: Incentivizing reasoning capability in LLMs via reinforcement learning. arXiv preprint arXiv:2501.12948 .

Huang, C., Tang, Z., Hu, S., Jiang, R., Zheng, X., Ge, D., Wang, B., Wang, Z., 2025. ORLM: A customizable framework in training large models for automated optimization modeling. *Operations Research*. Forthcoming.

Jiang, X., Wu, Y., Li, M., Cao, Z., Zhang, Y., 2025. Large language models as end-to-end combinatorial optimization solvers. arXiv preprint arXiv:2509.16865 .

Jiang, Z., Gu, J., Zhu, H., Pan, D., 2023. Pre-rmsnorm and pre-crmsnorm transformers: equivalent and efficient pre-ln transformers. *Advances in Neural Information Processing Systems* 36, 45777–45793.

Kool, W., Van Hoof, H., Welling, M., 2018. Attention, learn to solve routing problems! arXiv preprint arXiv:1803.08475 .

Kwon, Y.D., Choo, J., Kim, B., Yoon, I., Gwon, Y., Min, S., 2020. Pomo: Policy optimization with multiple optima for reinforcement learning. *Advances in Neural Information Processing Systems* 33, 21188–21198.

Liu, F., Lin, X., Wang, Z., Zhang, Q., Xialiang, T., Yuan, M., 2024. Multi-task learning for routing problem with cross-problem zero-shot generalization, in: Proceedings of the 30th ACM SIGKDD Conference on Knowledge Discovery and Data Mining, pp. 1898–1908.

Luo, F., Lin, X., Liu, F., Zhang, Q., Wang, Z., 2023. Neural combinatorial optimization with heavy decoder: Toward large scale generalization. *Advances in Neural Information Processing Systems* 36, 8845–8864.

Morandi, N., Leus, R., Yaman, H., 2024. The orienteering problem with drones. *Transportation Science* 58, 240–256.

Nguyen, E., Poli, M., Durrant, M.G., Kang, B., Katrekar, D., Li, D.B., Bartie, L.J., Thomas, A.W., King, S.H., Bixi, G., et al., 2024. Sequence modeling and design from molecular to genome scale with evo. *Science* 386, eado9336.

Oruc, B.E., Kara, B.Y., 2018. Post-disaster assessment routing problem. *Transportation Research Part B: Methodological* 116, 76–102.

Shazeer, N., 2020. Glu variants improve transformer. arXiv preprint arXiv:2002.05202 .

Shi, Y., Yang, J., Han, Q., Song, H., Guo, H., 2024. Optimal decision-making of post-disaster emergency material scheduling based on helicopter–truck–drone collaboration. *Omega* 127, 103104.

Steenbergen, R.M., Van Heeswijk, W.J., Mes, M., 2025. The stochastic dynamic postdisaster inventory allocation problem with trucks and uavs. *Transportation Science* 59, 360–390.

Touvron, H., Lavril, T., Izacard, G., Martinet, X., Lachaux, M.A., Lacroix, T., Rozière, B., Goyal, N., Hambro, E., Azhar, F., et al., 2023. Llama: Open and efficient foundation language models. arXiv preprint arXiv:2302.13971 .

Vaswani, A., Shazeer, N., Parmar, N., Uszkoreit, J., Jones, L., Gomez, A.N., Kaiser, L., Polosukhin, I., 2017. Attention is all you need, in: *Proceedings of the 31st International Conference on Neural Information Processing Systems*, pp. 5998–6008.

Vinyals, O., Fortunato, M., Jaitly, N., 2015. Pointer networks, in: *Proceedings of the 28th International Conference on Neural Information Processing Systems*, pp. 2692–2700.

Yin, Y., Yang, Y., Yu, Y., Wang, D., Cheng, T., 2023. Robust vehicle routing with drones under uncertain demands and truck travel times in humanitarian logistics. *Transportation Research Part B: Methodological* 174, 102781.

Zhang, B., Sennrich, R., 2019. Root mean square layer normalization. *Advances in neural information processing systems* 32.

Zhang, G., Jia, N., Zhu, N., Adulyasak, Y., Ma, S., 2023. Robust drone selective routing in humanitarian transportation network assessment. *European Journal of Operational Research* 305, 400–428.

Zhao, J., Mao, M., Zhao, X., Zou, J., 2020. A hybrid of deep reinforcement learning and local search for the vehicle routing problems. *IEEE Transactions on Intelligent Transportation Systems* 22, 7208–7218.

Zhou, J., Cao, Z., Wu, Y., Song, W., Ma, Y., Zhang, J., Xu, C., 2024. Mvmoe: Multi-task vehicle routing solver with mixture-of-experts. arXiv preprint arXiv:2405.01029 .

## A. Model component details

This appendix provides mathematical formulations for the key architectural components in Section 5.

**RMS** RMS normalization, originally introduced by Zhang and Sennrich (2019), provides improved training stability and reduced computational overhead compared to traditional instance normalization. In our encoder architecture, RMS normalization replaces instance normalization as described in Equation (3). For a given input vector  $\mathbf{x} \in \mathbb{R}^d$ , where  $d$  represents the embedding dimension, RMS normalization is computed as:

$$\text{RMS}(\mathbf{x}) = \frac{\mathbf{x}}{\sqrt{\frac{1}{d} \sum_{i=1}^d x_i^2 + \epsilon}} \odot \mathbf{g} \quad (\text{A1})$$

where  $\odot$  denotes element-wise multiplication,  $\mathbf{g} \in \mathbb{R}^d$  is a learnable scaling parameter vector, and  $\epsilon \approx 10^{-8}$  is a small constant introduced for numerical stability. Unlike instance normalization, RMS normalization eliminates the mean centering operation, thereby reducing computational complexity while maintaining normalization effectiveness. This modification is particularly beneficial for large-scale routing problems where computational efficiency is paramount.

**FA** FA optimizes memory usage and computational efficiency in attention mechanisms without sacrificing numerical accuracy (Dao et al. 2022, Dao 2023), as referenced in Equations (4) and (7). The standard MHA computation is given by:

$$\text{Attention}(\mathbf{Q}, \mathbf{K}, \mathbf{V}) = \text{softmax} \left( \frac{\mathbf{Q}\mathbf{K}^T}{\sqrt{d_k}} \right) \mathbf{V} \quad (\text{A2})$$

where  $\mathbf{Q} \in \mathbb{R}^{n \times d_q}$ ,  $\mathbf{K} \in \mathbb{R}^{n \times d_k}$ , and  $\mathbf{V} \in \mathbb{R}^{n \times d_v}$  denote the query, key, and value matrices, respectively. Here,  $n$  represents the sequence length, which corresponds to the number of nodes in our drone routing context, and  $d_q$ ,  $d_k$ , and  $d_v$  stand for the dimensions of the query, key, and value vectors, respectively. FA reformulates this computation using memory-efficient tiling and recomputation strategies:

$$\text{FA}(\mathbf{Q}, \mathbf{K}, \mathbf{V}) = \text{BlockwiseAttention}(\mathbf{Q}_{[1:B_q]}, \mathbf{K}_{[1:B_k]}, \mathbf{V}_{[1:B_v]}) \quad (\text{A3})$$

where  $B_q$ ,  $B_k$ , and  $B_v$  represent block sizes optimized for the memory hierarchy of the underlying hardware. This approach significantly reduces memory complexity from  $\mathcal{O}(n^2)$  to  $\mathcal{O}(n)$  for sequence length  $n$ , enabling efficient processing of large road networks with thousands of nodes.

**SGLUFFN** The SGLUFFN component, as defined in Equation (5), enhances the FFN’s expressiveness through an advanced gating mechanism. The Swish Gated Linear Unit activation function combines the benefits of gating with smooth activation properties. For input vector  $\mathbf{x} \in \mathbb{R}^d$ , the SGLUFFN transformation is computed as:

$$\text{SGLUFFN}(\mathbf{x}) = \text{Swish}(\mathbf{x}\mathbf{W}_1 + \mathbf{b}_1) \odot (\mathbf{x}\mathbf{W}_2 + \mathbf{b}_2) \quad (\text{A4})$$

where the Swish activation function is defined as:

$$\text{Swish}(\mathbf{z}) = \mathbf{z} \odot \sigma(\mathbf{z}) \quad (\text{A5})$$

and  $\sigma(\cdot)$  denotes the sigmoid function  $\sigma(z) = \frac{1}{1+e^{-z}}$ . The learnable parameters include transformation matrices  $\mathbf{W}_1, \mathbf{W}_2 \in \mathbb{R}^{d \times d_f}$  and bias vectors  $\mathbf{b}_1, \mathbf{b}_2 \in \mathbb{R}^{d_f}$ , where  $d_f$  represents the hidden dimension of the FFN. The gating mechanism ( $\odot$ ) enables the network to selectively emphasize or suppress different features, improving representational capacity compared to traditional ReLU-based FFN. This enhancement is particularly valuable for capturing complex non-linear relationships in drone routing optimization.

**SHA** SHA, as employed in Equation (8), simplifies the MHA mechanism for decoder operations where reduced complexity is beneficial while maintaining essential attention capabilities. For query vector  $\mathbf{q} \in \mathbb{R}^{d_q}$ , key matrix  $\mathbf{K} \in \mathbb{R}^{n \times d_k}$ , and value matrix  $\mathbf{V} \in \mathbb{R}^{n \times d_v}$ :

$$\text{SHA}(\mathbf{q}, \mathbf{K}, \mathbf{V}) = \text{softmax} \left( \frac{\mathbf{q}\mathbf{K}^T}{\sqrt{d_k}} \right) \mathbf{V}. \quad (\text{A6})$$

In our decoder architecture, SHA processes the context embedding  $\mathbf{h}_c^{(t)}$  with node representations to compute selection probabilities for the next node in the route.

**Softmax** The softmax function, as employed in Equation (9), converts raw attention scores into probability distributions for node selection during the decoding process. For a vector of logits  $\mathbf{u} = [u_0, u_1, \dots, u_n] \in \mathbb{R}^{n+1}$ , where  $u_i$  represents the unnormalized score for selecting node  $i$ :

$$\text{Softmax}(\mathbf{u}) = \frac{\exp(u_i)}{\sum_{j=0}^n \exp(u_j)}. \quad (\text{A7})$$

## B. Ablation study

We evaluate each architectural enhancement in the modern transformer encoder through controlled ablation experiments. Five variants are tested by replacing individual components with traditional alternatives while maintaining all others: (1) Base Group uses classical transformer with post-normalization, instance normalization, ReLU-based FFN, and standard attention; (2)

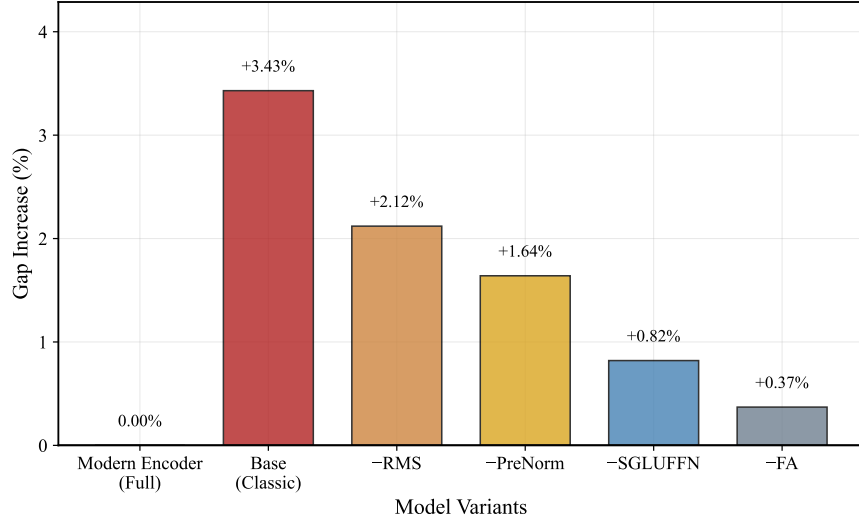


**Figure 8 Ablation Study Results Showing Optimality Gaps for Different Architectural Variants**

-RMS Group replaces RMS normalization with instance normalization; (3) -PreNorm Group uses post-normalization; (4) -SGLUFFN Group replaces SGLUFFN with ReLU-based FFN; (5) -FA Group uses standard attention.

Performance results measured by optimality gap relative to the full UM reveal significant component contributions. Figure 8 shows the ablation results across different problem instances. The Base Group with traditional components achieves the poorest performance, demonstrating substantial optimality gaps. Individual component removals show varying impacts: removing RMS normalization (-RMS) causes moderate performance degradation, while removing pre-normalization (-PreNorm) leads to more significant deterioration. The SGLUFFN activation function proves particularly critical, as its removal (-SGLUFFN) results in notable performance drops. FA removal (-FA) shows the least impact among individual components, though still measurable. These results validate our architectural choices and demonstrate that each modern component contributes meaningfully to the overall model performance.

## C. Mathematical formulation

This appendix presents the mathematical formulation for the PDRA problem, including attributes for different operational variants. The formulation serves as the basis for commercial solver implementation using Gurobi.

**Basic model formulation** Let  $x_{ij}^k$  be the binary decision variable indicating whether drone  $k$  traverses link  $(i, j)$  for assessment, where  $x_{ij}^k = 1$  if drone  $k$  flies the link, and  $x_{ij}^k = 0$  otherwise. The PDRA-Basic model is formulated as (Gong et al. 2025):

$$\max_{k \in K} \sum_{p \in P} c_p \left( \sum_{j:(p,j) \in \bar{A}} x_{pj}^k \right) \quad (C1)$$

$$\text{s.t.} \quad \sum_{k \in K} \sum_{j:(p,j) \in \bar{A}} x_{pj}^k \leq 1 \quad \forall p \in P \quad (C2)$$

$$\sum_{j \in \bar{N}} x_{ji}^k = \sum_{j \in \bar{N}} x_{ij}^k \quad \forall i \in \bar{N}, \forall k \in K \quad (C3)$$

$$\sum_{j \in \bar{N}} x_{oj}^k = \sum_{i \in \bar{N}} x_{io}^k = 1 \quad \forall k \in K \quad (C4)$$

$$\sum_{(i,j) \in \bar{A}} t_{ij} x_{ij}^k \leq Q \quad \forall k \in K \quad (C5)$$

$$\max_{k \in K} \left\{ \sum_{(i,j) \in \bar{A}} t_{ij} x_{ij}^k \right\} \leq p_{\max} \quad (C6)$$

$$u_i^k + 1 - u_j^k \leq M(1 - x_{ij}^k) \quad \forall (i,j) \in \bar{A}, \forall k \in K \quad (C7)$$

$$x_{ij}^k \in \{0, 1\} \quad \forall (i,j) \in \bar{A}, \forall k \in K \quad (C8)$$

$$u_i^k \in \{1, 2, \dots, |\bar{N}|\} \quad \forall i \in \bar{N}, \forall k \in K \quad (C9)$$

where:

- Equation (C1): Maximize total information value collected from artificial nodes  $P$
- Equation (C2): Each artificial node visited by at most one drone (no redundant assessment)
- Equation (C3): Flow conservation constraint ensuring path continuity
- Equation (C4): Each drone starts and ends at depot  $o$
- Equation (C5): Flight time constraint within battery limit  $Q$
- Equation (C6): Maximum allowable assessment time constraint within limit  $p_{\max}$
- Equation (C7): Miller-Tucker-Zemlin subtour elimination constraint with  $M = |\bar{N}|$
- Equations (C8)–(C9): Variable domain constraints

**OR attribute** For the open route configuration where drones do not return to depot:

$$t_{io} = 0 \quad \forall i \in \bar{N}. \quad (C10)$$

This modification eliminates return-to-depot time costs, allowing drones to terminate routes at any feasible location.

#### **TW attribute Additional Variables:**

- $a_i^k$ : Arrival time of drone  $k$  at node  $i$
- $l_i$ : Latest allowable arrival time at node  $i$

**Additional Constraints:**

$$a_i^k \leq l_i \quad \forall i \in \bar{N}, \forall k \in K \quad (C11)$$

$$a_j^k \geq a_i^k + t_{ij} - M(1 - x_{ij}^k) \quad \forall (i, j) \in \bar{A}, \forall k \in K \quad (C12)$$

$$a_o^k = 0 \quad \forall k \in K \quad (C13)$$

$$a_i^k \geq 0 \quad \forall i \in \bar{N}, \forall k \in K \quad (C14)$$

where Equation (C11) enforces time window compliance, Equation (C12) ensures time continuity along paths, Equation (C13) sets depot departure time, and Equation (C14) maintains temporal feasibility.

**MD attribute Additional Variables:**

- $z_o^k$ : Binary variable indicating drone  $k$  assignment to depot  $o \in \mathcal{D}$
- $\mathcal{D}$ : Set of origin depots
- $\delta_o$ : Capacity (maximum drones) at depot  $o$

**Additional Constraints:**

$$\sum_{o \in \mathcal{D}} z_o^k \leq 1 \quad \forall k \in K \quad (C15)$$

$$\sum_{j \in \bar{N}} x_{oj}^k \leq z_o^k \quad \forall o \in \mathcal{D}, \forall k \in K \quad (C16)$$

$$\sum_{k \in K} z_o^k \leq \delta_o \quad \forall o \in \mathcal{D} \quad (C17)$$

$$\sum_{j \in \bar{N}} x_{jo}^k = z_o^k \quad \forall d = o \in \mathcal{D}, \forall k \in K \quad (C18)$$

$$z_o^k \in \{0, 1\} \quad \forall o \in \mathcal{D}, \forall k \in K \quad (C19)$$

where Equation (C15) assigns each drone to at most one depot, Equation (C16) links depot assignment to path decisions, Equation (C17) enforces depot capacity, Equation (C18) ensures return to assigned depot, and Equation (C19) defines binary depot assignment variables.

**Implementation notes Model Variants:** The eight PDRA variants are obtained by combining the attributes:

- PDRA-Basic: Equations (C1)–(C9)
- PDRA-OR: Add Equation (C10)
- PDRA-TW: Add Equations (C11)–(C14)
- PDRA-OR-TW: Add Equations (C10)–(C14)
- PDRA-MD: Add Equations (C15)–(C19)
- PDRA-OR-MD: Add Equations (C10), (C15)–(C19)
- PDRA-TW-MD: Add Equations (C11)–(C19)
- PDRA-OR-TW-MD: Add all attribute equations.